buildings

MDPI

Article

Assessment of Contact Laws Accounting for Softening in 3D Rigid Concrete Particle Models

Nuno Monteiro Azevedo *, Maria Luísa Braga Farinha and Sérgio Oliveira

Concrete Dams Department, National Laboratory for Civil Engineering (LNEC), 1700-066 Lisboa, Portugal; lbraga@lnec.pt (M.L.B.F.); soliveira@lnec.pt (S.O.)

* Correspondence: nazevedo@lnec.pt; Tel.: +351-218443368

Abstract: To obtain predictions closer to concrete behaviour, it is necessary to employ a particle model (PM) that considers contact softening. A bilinear softening contact model (BL) has been adopted in PM studies. Several limitations in PM predictions have been identified that may be due to BL assumptions. For this reason, this paper compares BL predictions with those obtained with more complex models to assess if PM predictions can be improved. As shown, it is possible to calibrate each contact model to reproduce the complex behaviour observed in concrete in uniaxial and biaxial loading. The predicted responses are similar, and the known PM limitations still occur independently of the adopted model. Under biaxial loading, it is shown that a response closer to that observed in concrete can be obtained (higher normal-to-stiffness ratio of ≈0.50, maximum contact compressive strength of ≈60 MPa, and 30% reduction in the number of working contacts). The BL contact model for PM concrete DEM-based simulations is shown to have (i) lower associated computational costs (15% to 50% lower); (ii) a reduced number of contact strength parameters; and (iii) similar responses to those predicted with more complex models. This paper highlights that the BL contact model can be used with confidence in PM fracture studies.

Keywords: particle model; discrete element; contact softening laws; concrete fracture

Citation: Azevedo, N.M.; Farinha, M.L.B.; Oliveira, S. Assessment of Contact Laws Accounting for Softening in 3D Rigid Concrete Particle Models. *Buildings* **2024**, *14*, 801. https://doi.org/10.3390/buildings14030801

Academic Editor: Cedric Payan

Received: 27 February 2024
Revised: 11 March 2024
Accepted: 13 March 2024
Published: 15 March 2024

1. Introduction

Detailed rigid particle models (PMs) based on the discrete element method (DEM) that take directly into account the material grain structure, namely, its randomness and its internal length, and the physical mechanisms of particle interaction can predict cracking phenomena in quasi-brittle materials and have gained relevance in rock [1–5], concrete [6–10], reinforced concrete [11,12], masonry [13,14], and asphalt mixtures [15,16]. DEM-based PM models have also been shown to be an effective tool for understanding the effect of particle shape and size on the macroscopic behaviour of granular materials and clays [17,18].

Meshless-based particle models based on a continuum framework, such as smoothed Particle Hydrodynamics (SPH) [19] or the material point method [20] have been proposed for concrete fracture. Still, the heterogeneous internal structure of concrete, which is composed of aggregates of different sizes embedded in a cement matrix with different phases and pores, favours the adoption of discrete-based particle models.

Regarding DEM-based particle models (PMs) for concrete, most of the research has been focused on generating PMs closer to the real concrete structure using, for example, X-ray computed tomography (XCT) [21–23], or focused on considering more complex aggregate shapes, either through particle clusters [10] or polyhedra [24], that can either be rigid or flexible. Very few studies have focused on the importance of the adopted contact models [6]. To obtain predictions closer to experimental observations in concrete, it may be necessary to employ a PM that accounts for softening at the contact level [6,7,9,10]. When employing a brittle contact model, the concrete heterogeneity at the meso-level needs to be included with greater detail, which significantly increases the associated computational

costs. Such refined particle models have primarily found application in 2D simulations [25] or in 3D simulations through the adoption of higher minimum particle content thresholds for the aggregate and mortar components [8,22].

In the early works of meso-modelling, namely, in lattice models [26] or in the combined beam-particle model [27], which are detailed PMs that adopt particle interaction and solution schemes different from a DEM-based PMs, a brittle contact model was usually considered. Nowadays, there is still a discussion in the particle modelling community on whether the contact model should be as simple as possible (brittle model) and whether the macroscopic behaviour should be an emergent property of the heterogeneity included in the PM or if more complex contact models should be adopted, such as linear or bilinear softening models, in order to predict a response in better agreement with the known concrete behaviour, with lower discretization requirements (particle refinement and material heterogeneity). Examples of the latter can be found in the early PM proposed in [28], in 3D modelling using the rigid body spring method (RBSM) [29,30], and in DEM-based PMs that adopt either a non-physical [7] or a physical representation of concrete [6,8–10].

A PM that includes a 3D contact model (VGCM-3D), which enables moment transmission through the contact surface, approximates polyhedral particle shapes and uses a bilinear softening contact model (BL), has been proposed [31]. Through these features, the PM has been shown to accurately replicate the ratio of compressive strength to tensile strength, as well as the ratio of direct tensile strength to indirect tensile strength typically observed in hard rock specimens [31]. Several limitations in PM predictions have been identified that may be due to BL assumptions, namely, with the BL contact model, a clear two-slope curve is predicted under uniaxial compression for a hard rock [31].

A 3D lattice discrete particle model (LDPM) that only considers larger aggregate particles and adopts softening/hardening contact laws based on a stress–strain boundary concept (LSSB) has been proposed for concrete fracture modelling [32]. Contrary to the LDPM model, the particle modelling approach here adopted also includes the particles representing the mortar, allowing for a more realistic representation of concrete, and updates contacts as the calculation progresses, allowing the PM to be applied to large deformation problems. A PM that only adopts the larger aggregate sizes embedded in a matrix phase using a 3D finite element model (FEM) and considers for the zero-thickness interface finite elements a cohesive fracture constitutive model (CFM) has also been proposed for concrete fracture studies [33]. Compared with the detailed particle modelling approach here adopted, the PM-based FEM model has a significant associated computational cost, and for this reason, it has only been applied in smaller geometries, only considering a few coarse aggregates [34]. In this work, BL predictions are compared with those obtained with more complex models [32,33] to assess if PM predictions can be improved.

The performance of the constitutive contact models [6,32,33] is initially compared for a single contact in tensile, pure shear, shear under uniaxial loading, and mixed mode, which are contact force trajectories that may occur in the contacts of a PM concrete model under complex loading. Additionally, uniaxial tensile and uniaxial compression tests and biaxial tests are presented. The predicted macroscopic response of the different constitutive models is compared. Several parametric studies are also carried out to assess if the contact model agreement with the known concrete biaxial behaviour can be improved.

It is shown that the macroscopic response predicted with the contact models under assessment is similar but requires, for each contact model, the adoption of a different set of best-fit calibration properties, which are model-dependent. For all contact models, it is shown that a better agreement with the known concrete biaxial compressive loading failure envelope can be obtained if (i) the normal to shear stiffness is increased to ≈0.50; (ii) the number of working contacts is reduced in 30%; and (iii) a maximum contact compressive strength of 60.0 MPa is adopted. A two-step calibration procedure that greatly reduces the required computational time can be adopted with all the softening based contact models.

This paper shows that the BL contact model can be used with confidence in PM fracture studies. The BL contact model has the following advantages when adopted in detailed 3D PM DEM based models: (i) a fewer number of contact parameters requiring calibration, (ii) substantially reduced associated computational costs, and (iii) for the best-fit properties found using uniaxial tests, it provides the best agreement with concrete-observed biaxial behaviour. To enhance the agreement with known concrete behaviour under biaxial loading, a compression cap needs to be included in the BL model.

The LSSB contact model is also shown to be a viable alternative for concrete fracture studies, with the advantage of including a stress–strain boundary for high compressive stresses. However, the LSSB contact model computational costs are much higher than those associated with the BL contact model. The CFM contact model is the most challenging model to implement within a DEM-based PM. It also requires the consideration of a compression cap and needs, for the best agreement with concrete biaxial behaviour, a normal to shear stiffness ratio closer to 1.0, which cannot be adopted in PM studies if Poisson's ratio is to be properly approximated.

2. Discrete Element-Based Particle Model

2.1. Basics

In a discrete element-based PM, the domain is divided into an assembly of particles that interact through contact interfaces. The DEM is based on the following two main assumptions: (i) the set of forces acting on each particle are related to the relative displacements of the particle to its neighbours and given the applied forces and (ii) Newton's law of motion is applied to define the new particle position. In each calculation step, given the forces applied at each particle, the new positions and velocities are calculated based on Newton's second law. The equations of motion are given by:

$$F_i(t) + F_i^d(t) = m\ddot{x}_i \tag{1}$$

$$M_i(t) + M_i^d(t) = I\dot{\omega}_i \tag{2}$$

where $F_i(t)$ and $M_i(t)$ correspond, respectively, to the total force and total momentum applied at instant t, $F_i^d(t)$ and $M_i^d(t)$ correspond, respectively, to the damping force and damping momentum applied at instant t, m and I correspond to the mass and inertia of the particle, $\ddot{x}_i$ is the acceleration of the particle, and $\dot{\omega}_i$ is the angular acceleration of the particle. Equation (2) represents the equation of rotational motion for a spherical particle. If the angular velocities are relevant and the particles are not spherical, it is necessary to use a more complex approach, given the non-linear nature of the equations of rotational motion. In the simulations presented, it is not relevant to perform a correct integration of the particles' rotational movement given that a quasi-static regime based on a scaled mass algorithm is adopted and the particles' geometries are closer to a sphere, which greatly reduces the angular motion relevance. Also, the adopted PM are compact assemblies where each particle has a high number of interactions with neighbouring particles, which also limits the relevance of the angular motion. In a dynamic analysis, under high strain rates and in highly fractured models, with irregular polyhedral particles, the correct integration of the rotational equations would be paramount. In the uniaxial tests here presented, a local non-viscous damping approach with a local damping value of 0.70 was adopted [35]. The uniaxial tests were carried out under displacement control, adopting a constant plate velocity that assures quasi-static loading conditions. An adaptive dynamic relaxation viscous damping (ADR) approach was adopted in the biaxial tests that were carried out under load control. When compared with a local damping approach, an ADR approach allows for larger loading steps to be adopted and faster convergence rates, making this approach more suitable when only peak load values are required [6].

2.2. Voronoi-Generalized Contact Model (VGCM-3D)

A 3D Voronoi-generalized contact model (VGCM-3D) was adopted, where both the contact surface and the contact location are determined through the Laguerre–Voronoi tessellation of the gravity centres of the interacting spherical particles [31], as shown in Figure 1. Laguerre–Voronoi diagrams are constructed based on a weighted metric, which considers the radius of the spherical particle associated with its gravity centre point. Thus, the facets of Laguerre–Voronoi diagrams are equidistant from the associated spheres, while the facets associated with simple Voronoi diagrams are equidistant from their gravity centres. A Laguerre–Voronoi tessellation was chosen because, compared with Voronoi tessellation, the facets are closer to the contact location adopted in the single point contact model (PCM) usually adopted in the DEM modelling of spherical particles, that is, at half the distance between the spherical particles [1].

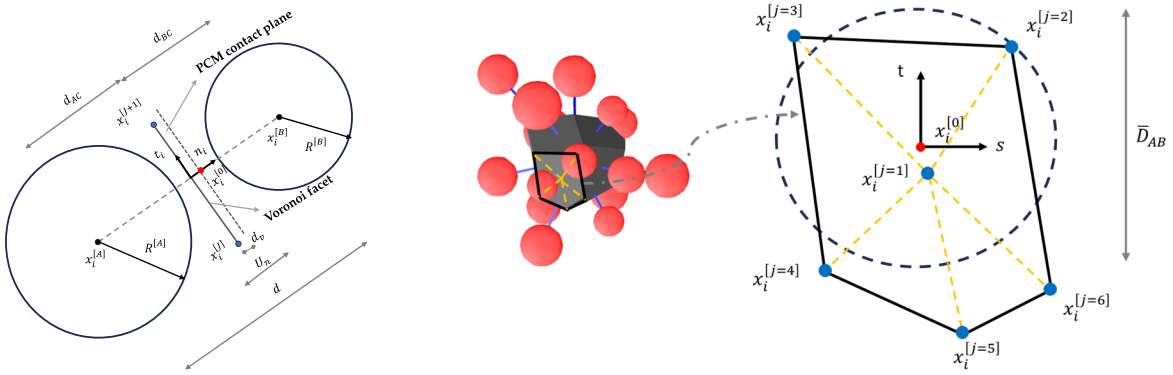

Figure 1. VGCM-3D contact model. Local points are defined according to the vertices of the Laguerre–Voronoi facet and its centre of gravity: (**a**) (t, n) plane and (**b**) (t, s) plane.

The local contact point locations, where force transmission occurs between two interacting particles through normal and shear springs, as shown in Figure 1b, are given by the common Laguerre–Voronoi facet vertexes including its gravity centre. As shown in Figure 1b, the VGCM-3D contact model considers, in an approximate way, the polyhedral shaped particles associated with the Laguerre–Voronoi cells. The advantage of a PM model that adopts a VGCM-3D contact over complex polyhedral-based PMs [24] lies in its ability to maintain the simplicity of spherical particle PMs while avoiding the need for a substantial increase in computational effort compared to the traditional PCM [1]. The contact location and the contact unit normal are still defined as if the particles are spherical, whereas in complex polyhedral interactions, the contact detection and resolution is a much more complex geometric problem.

Similar to the PCM [1], in the VGCM-3D contact model, the contact unit normal (n_i) is defined based on the centre of gravity of the interacting particles and on the distance between the particle gravity centres (d). The contact overlap (U_n) also follows the usual PCM approach [1]. The reference contact point defined at the Laguerre–Voronoi facet is given by:

$$x_i^{[0]} = x_i^{[A]} + \left(R^{[A]} - \frac{1}{2} U_n - d_v \right) n_i \tag{3}$$

where d_v is the distance, in the direction normal to the contact plane, between the contact plane usually adopted between two spherical particles in a PCM and the contact plane defined by the Laguerre–Voronoi facet (Figure 1a).

The novelty of the VGCM-3D contact model is that the local contact points correspond initially to the vertices of the Laguerre–Voronoi facet. The position of each local contact point ($x_i^{[J]}$) in global coordinates is defined based on the relative position of the local point in a local reference frame (t,s) centred on the reference contact point (Figure 1b). The relative

positions are defined at the start of the simulation considering the global coordinates of each vertex of the Voronoi facet and the global coordinates of the reference point. Thus, at each calculation step, the position of each local point in global coordinates is given by:

$$x_i^{[J]} = x_i^{[0]} + s^{[J]} x_i^{[s]} + t^{[J]} x_i^{[t]} \tag{4}$$

where $x_i^{[s]}$ and $x_i^{[t]}$ are, respectively, the local coordinates along the local axis s and the local axis t, defined on the global coordinate axis, based on $\vec{s} \times \vec{t} = \vec{n}$. Given the normal ($k_n^{[J]}$) and shear local contact point stiffness ($k_s^{[J]}$), the normal and shear local contact force increments are obtained following an incremental linear law:

$$\Delta F^{[J,N]} = -k_n^{[J]} \Delta x^{[J,N]} = -k_n^{[J]} \left(\dot{x}_i^{[J]} \Delta t \right) n_i \tag{5}$$

$$\Delta F_i^{[J,S]} = -k_s^{[J]} \Delta x_i^{[J,S]} = -k_s^{[J]} \left(\dot{x}_i^{[J]} \Delta t \right) - \Delta x^{[J,N]} n_i \tag{6}$$

where $\Delta x^{[J,N]}$ is the local contact displacement normal increment (scalar) and $\Delta x_i^{[J,S]}$ is the local contact shear displacement increment (vector). Additional details of the VGCM-3D contact model can be found in [31].

2.3. Local Contact Stiffness and Strength

In this study, the contact stiffness at each local contact point within the VGCM-3D model is determined by the Young's modulus of the equivalent continuum material ($\overline{E}$) and by a constant that correlates the local contact point normal and shear stiffnesses spring values (α):

$$k_n^{[J]} = \frac{\overline{E}}{d} A_c^{[J]} \tag{7}$$

$$k_s^{[J]} = \alpha \, k_n^{[J]} \tag{8}$$

where $A_c^{[J]}$ is the contact area of local point J and d is the distance between the particles' centres of gravity. The maximum tensile and shear strength properties are established given the maximum contact tensile stress ($\sigma_{n.t}$), the maximum contact cohesion stress (τ), and the local contact point area ($A_c^{[J]}$):

$$F_{n.max}^{[J]} = \sigma_{n.t} \, A_c^{[J]} \tag{9}$$

$$C_{max}^{[J]} = \tau \, A_c^{[J]} \tag{10}$$

2.4. PM Generation

Figure 2 shows the adopted PM generation procedure for the tensile tests that are assessed in Section 3. The aggregate content, comprising particle dimensions ranging from 4.0 to 8.0 mm in diameter and from 8.0 to 16.0 mm in diameter, which represent 44% of the total volume of the aggregate size distribution [36], is considered in the PM. The aggregate particles are inserted from the highest to the smallest particle diameter. The particles representing the mortar are subsequently introduced adopting a porosity value of 0.1 and a uniform distribution, featuring diameters ranging between 4.0 and 5.0 mm [6].

Next, the centres of gravity of the spherical particles are triangularized based on a weighted Delaunay algorithm. The associated Laguerre–Voronoi diagram is then constructed from the weighted Delaunay tetrahedra structure. Figure 2c presents the Laguerre–Voronoi cells of the aggregate particles with 8.0 to 16.0 mm. As mentioned, the VGCM-3D contact between two neighbouring particles is established given the associated Laguerre–Voronoi facet [31]. The adopted PM generation scheme promotes an increase in the number of contacts per particle and allows for moment transmission, which leads to a better agreement with known experimental results in hard rock [31]. A comprehensive review of DEM-based concrete model generation approaches can be found in [37].

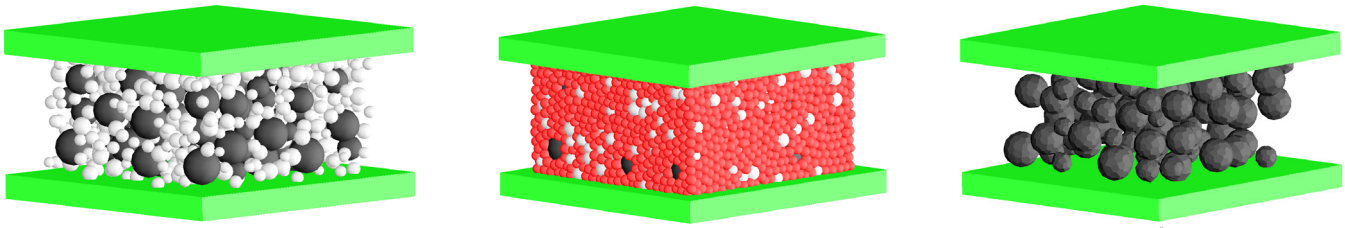

(**a**) (**b**) (**c**)

Figure 2. PM generation steps for concrete: (**a**) aggregate particle insertion: particles with 8.0 to 16.0 diameter (black) and particles with 4.0 to 8.0 mm diameter (light grey); (**b**) compact assembly with particles with 4.0 to 5.0 mm diameter representing the mortar (red); and (**c**) Laguerre–Voronoi cells of the aggregate particles with 8.0 to 16.0 mm diameters.

2.5. Contact Softening Models

2.5.1. Vectorial Simplified Softening Contact Model (BL)

A vectorial bilinear softening contact model for both normal and shear directions has been introduced for concrete fracture studies in particle modelling [6,12], as depicted in Figure 3. The incorporation of linear/bilinear softening contact models increases the performance of PM, namely, under tensile loading [6,12]. The BL contact model's simplicity facilitates its implementation in particle modelling. The force/displacement relationships are straightforwardly established based on the maximum contact tensile stress, the maximum cohesion stress, and the contact fracture energies in mode I ($G_{f.n}$) and mode II ($G_{f.s}$). Damage in each direction is quantified as a function of the maximum displacement experienced by the contact in that direction, Figure 3. In an approximate way, the local contact point damage is given by the sum of the tensile and shear damages. Given the current total contact damage, the maximum values of tensile and cohesive strengths are reduced accordingly, and the contact forces are corrected given the updated maximum strength values. With the current contact damage assessed, the maximum values of tensile and cohesive strengths are adjusted, and the contact forces are recalibrated according to the revised maximum strength values.

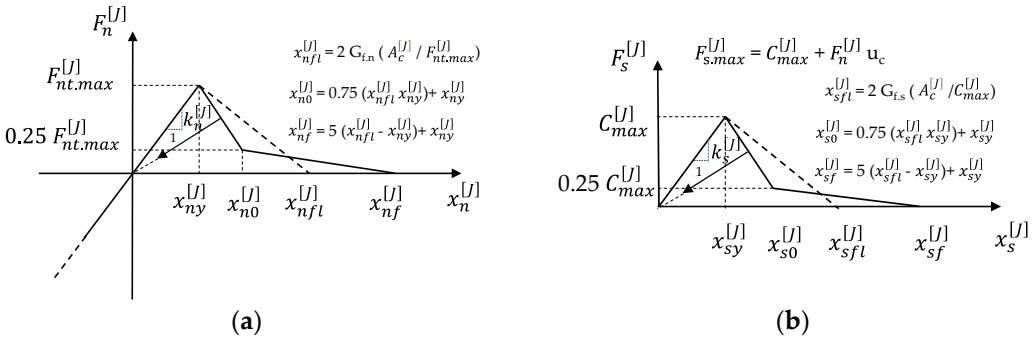

(**a**) (**b**)

Figure 3. Bilinear vectorial softening contact model (BL): (**a**) normal direction and (**b**) shear direction.

2.5.2. Lattice Discrete Particle Stress–Strain Boundary-Based Contact Model (LSSB)

A contact constitutive model based on the concept of the stress–strain boundary has been proposed for concrete fracture within the framework of a 3D lattice discrete-based PM [32]. Note that, the stress–strain boundary concept is introduced in [38] for microplane model M3, which is a continuous approach that has some similarities with the PMs, namely, through its concept of integrating the constitutive laws in several directions on a unit sphere.

The lattice discrete particle stress–strain boundary-based contact model (LSSB) is based on a stress–strain boundary that is defined as a function of the equivalent contact stress (σ_{eq}) given by:

$$\sigma_{eq} = \sqrt{\left(\sigma_n^{[J]}\right)^2 + \frac{\left(\tau_s{}^{[J]}\right)^2}{\alpha}} \tag{11}$$

The local contact point normal stress, $\sigma_n^{[J]}$, and the local point contact shear stress, $\tau_s{}^{[J]}$, are set given the local contact point normal ($F_n^{[J]}$) and shear ($F_s^{[J]}$) forces and given the local point contact area ($A_c^{[J]}$).

The equivalent stress–strain boundary enables the simulation of weakening and hardening behaviours based on the equivalent contact stress state. The stress–strain boundary is characterized by the effective strain (ε) and the coupling variable (ω) and it is mathematically expressed through the function:

$$\sigma_b(\varepsilon, \omega) = \sigma_0(\omega)\exp\left\{\frac{K(\omega)}{\sigma_0(\omega)}\langle\varepsilon_1(\varepsilon, \omega) - \varepsilon_0(\varepsilon, \omega)\rangle\right\} \tag{12}$$

where $\langle\varepsilon_1(\varepsilon, \omega) - \varepsilon_0(\varepsilon, \omega)\rangle = \max\{\varepsilon_1(\varepsilon, \omega) - \varepsilon_0(\varepsilon, \omega),\ 0\}\}$. The function $\varepsilon_0(\varepsilon, \omega)$ denotes the deformation limit beyond which the boundary is no longer equal to $\sigma_0(\omega)$ but has changed exponentially as a function of $\varepsilon_1(\varepsilon, \omega) - \varepsilon_0(\varepsilon, \omega)$. The effective strain ($\varepsilon$) is determined by the expression:

$$\varepsilon = \sqrt{\left(\varepsilon_n{}^{[J]}\right)^2 + \alpha\ \left(\varepsilon_s{}^{[J]}\right)^2} \tag{13}$$

where the effective normal strain ($\varepsilon_n{}^{[J]}$) and the tangential strain ($\varepsilon_s{}^{[J]}$) are derived from the normal ($x_n{}^{[J]}$) and shear ($x_s{}^{[J]}$) displacements at the local contact point, as well as the inter-particle distance (d):

$$\varepsilon_n{}^{[J]} = \frac{x_n{}^{[J]}}{d};\ \varepsilon_s{}^{[J]} = \frac{\left\|x_s{}^{[J]}\right\|}{d} \tag{14}$$

Figure 4a shows the function $\sigma_0(\omega)$, which represents the boundary in the (σ, τ_s) plane:

$$\sigma_0(\omega) = \begin{cases} \sigma_{01}(\omega) & \text{if} \quad \omega \leq \omega_0 \\ \sigma_{02}(\omega) & \text{if} \quad \omega > \omega_0 \end{cases} \tag{15}$$

where $\tan\omega_0 = \frac{\sigma_0}{\tau/\sqrt{\alpha}}$ represents the point at which the two curves intersect, as shown in Figure 4a, which is associated with the angle of internal friction of the LSSB contact model. The function $\sigma_{01}(\omega)$ represents the stress–strain boundary for high compressive stress states and is characterized by an elliptical function:

$$\left(\sigma_n^{[J]}\right)^2 + \frac{\left(\tau_s{}^{[J]}\right)^2}{\beta} = {\sigma_c}^2 \tag{16}$$

where σ_c is the maximum contact compressive stress at the contact. A value of β equal to 1.0 is considered in this work. In [32], the value of β is defined by setting an expression in terms of the confinement stress, which is approximated by the average stress value at the contact location. The stress at each particle can be approximated given the contact forces [1,27].

The function $\sigma_{02}(\omega)$ defines the stress–strain boundary for both the tensile/shear and compressive/shear stress states, expressed through a hyperbolic function, which correlates the shear stress at the contact ($\tau_s{}^{[J]}$) with the normal stress at the contact ($\sigma_n^{[J]}$) considering:

$$\tau_s{}^{[J]} = \mu_1\sqrt{\left(\sigma_n^{[J]} - \sigma_{n.t} - \sigma_a\right)^2 - {\sigma_a}^2} \tag{17}$$

where μ_1 is the slope of the function $\sigma_{02}(\omega)$ asymptote at the intersection point with the function $\sigma_{01}(\omega)$ and σ_a is given by:

$$\sigma_a = \frac{\sigma_{n.t}}{2}\left[\left(\frac{2}{\mu_1\,\tau}\right)^2 - 1\right] \tag{18}$$

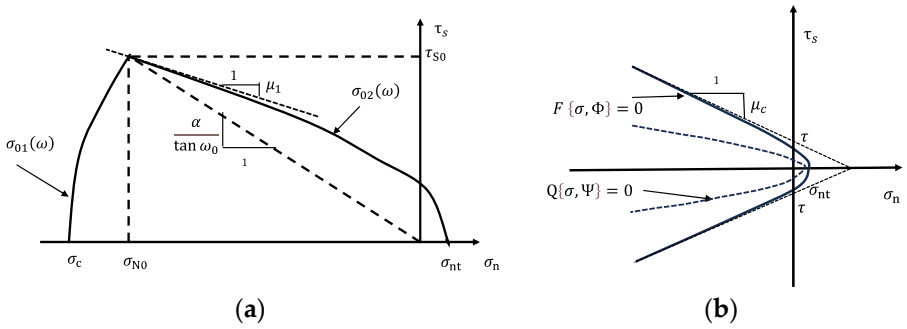

Figure 4. Lattice discrete particle stress–strain boundary-based contact model (LSSB) and Cohesive fracture constitutive model (CFM): (**a**) LSSB stress–strain boundary and (**b**) CFM hyperbolic loading surface ($F\{\sigma,\Phi\}=0$) and plastic potential ($Q\{\sigma,\Psi\}=0$).

The LSSB contact model has been shown to effectively capture concrete behaviour under complex loading conditions [32], even with a coarser particle model (PM). Additional details about the implementation of the LSSB model can be found in [32]. A more complex LSSB model has been proposed that can handle pore collapse and material compaction [39]. Unlike the BL contact model, the LSSB contact model incorporates a stress–strain boundary for high contact compression values, and the contact friction angle functions is an internal variable determined by the following expression:

$$\varphi = \arctan\left(\frac{\alpha}{\tan\omega_0}\right) \tag{19}$$

2.5.3. Cohesive Fracture Constitutive Model (CFM)

Within the framework of particle modelling, a cohesive fracture constitutive model (CFM) has been proposed, where concrete is represented by the larger aggregate sizes embedded within a matrix phase. In this PM, both the aggregate particles and the matrix deformability are represented through an internal finite element tetrahedral mesh [33,34].

In this cohesive fracture constitutive model, cracking behaviour is characterized by a hyperbolic function, that enables a smooth transition from tensile to shear cracking. The yield surface in terms of maximum tensile stress, cohesion, and a frictional term is represented by:

$$F\{\sigma,\Phi\} = \left(\tau_s{}^{[J]}\right)^2 - \left(\tau - \sigma_n^{[J]}\,\mu_c\right)^2 + \left(\tau - \sigma_{n.t}\,\mu_c\right)^2 = 0 \tag{20}$$

The plasticity potential is likewise represented by a hyperbolic function that is defined given the maximum tensile stress, an apparent cohesion term (τ_Q), and an apparent friction term (μ_{cQ}):

$$Q\{\sigma,\Psi\} = \left(\tau_Q - \sigma_{n.t}\,\mu_{cQ}\right) + \sqrt[2]{\left(\tau_s{}^J\right)^2 + \left(\tau_Q - \sigma_{n.t}\,\mu_{cQ}\right)^2} = 0 \tag{21}$$

In this way, contrary to the BL and LSSB contact models, the CFM contact model allows for the adoption of non-associated formulations that in continuum macroscopic analysis are required to successfully model materials like concrete that have a significant pressure sensitivity behaviour. The evolution of this surface is governed by an internal variable (W_{CR}), which is determined by the work performed during the fracture process:

$$d\,W_{CR} = \begin{cases} \sigma_n^{[J]} dx_{n.crack}{}^{[J]} & \sigma_n^{[J]} \geq 0 \quad (tension) \\ \left(\tau_s{}^{[J]} + \sigma_n^{[J]}\,\mu_c\right) d\left\|x_{s.crack}{}^{[J]}\right\| & \sigma_n^{[J]} < 0 \quad (compression) \end{cases} \tag{22}$$

The evolution of the maximum tensile stress, cohesion, and the frictional term is defined as a function of the internal variable (W_{CR}) and of the values of fracture energy in mode I ($G_{f.n}$) and mode II ($G_{f.s}$). Further specifics regarding the CFM model's implementation are detailed in [33].

2.5.4. Summary of the Three Different Contact Models

Three contact softening models have been briefly described. The BL contact model is vectorial-based and requires the definition of the following five strength properties: the maximum tensile strength ($\sigma_{n.t}$), the contact energy in mode I ($G_{f.n}$), the maximum cohesion stress (τ), the contact friction term (μ_c), and the fracture energy in mode II ($G_{f.s}$). Several limitations in PM predictions have been identified that may be due to BL assumptions. For this reason, this paper compares BL predictions with those obtained with more complex models that have been adopted with success in coarser PMs including the LSSB and the CFM contact models.

The LSSB contact model is an analytical model based on the evolution of a stress–strain boundary. Noteworthy, to ensure that the adopted fracture energy in tension and pure shear is respected and that the stress–boundary equations are mathematically sound, the contact input values have to follow some rules and are interconnected, which may limit the application of the LSSB model to materials other than concrete [26]. Compared with the BL contact model, the LSSB has the following additional strength parameter: the maximum compression contact strength that controls the evolution of the stress–strain boundary for higher contact compressive forces. The model is defined in terms of stress/strain parameters that are approximated given the contact forces and contact displacements, and its implementation within a PM is straightforward.

The CFM contact model is a cohesive fracture constitutive model that adopts hyperbolic functions to represent the cracking surface and the plastic potential. The CFM is defined in terms of stress values that are approximated given the contact forces and the contact area. Its implementation within a PM is challenging given that it requires the numerical integration of the constitutive equations. It is the most complex model under assessment, allowing for dilatancy and the reduction of the frictional term with damage increase. If a non-associated formulation is adopted, the model requires, when compared with the BL contact model, the definition of three additional contact strength parameters as follows: an apparent cohesion term (τ_Q), an apparent friction term (μ_{cQ}) and a residual contact friction term (μ_{cr}).

3. Application Examples

3.1. Methodology

The three contact models under assessment were initially evaluated for a single contact for different loading conditions, which attempt to simulate possible contact force evolutions that may occur in a PM assembly.

In the following, for each contact model, the best-fit contact properties that predict the best agreement with known concrete behaviour under uniaxial and compression loading using a trial-and-error procedure are presented. With this task, it will be possible to compare the best-fit predictions obtained with each model and to assess the best-fit strength property values of each contact model. For the best-fit contact strength properties, the biaxial response predicted by each contact model is compared.

Additionally, the following parametric studies are also presented to improve the contact models' biaxial failure envelope predictions and to evaluate if the tendencies and behaviour of each contact model under assessment follow similar trends:

- Normal to shear stiffness ratio (α) of 0.50;
- A 30% reduction in the PM total number of contacts;
- Maximum compressive contact strength of 60.0 MPa;
- Single-point contact model (PCM);
- PM refinement.

3.2. Single VGCM-3D Contact

The behaviour of a single VGCM-3D contact under tensile loading (T), under shear loading with an initial imposed axial stress (S&A), and under mixed loading (HMM) was assessed by adopting the presented constitutive models that include softening at the contact level, as shown in Figure 5. The tensile test (T) was performed under displacement control by applying a vertical velocity at the upper spherical particle, and the shear test with an initial imposed axial force (S&A) was performed by setting, in a first stage, axial contact stress and, after reaching the equilibrium, horizontal velocity is imposed on the upper particle. The mixed loading test (HMM) attempts to model the experiment developed in [40] for concrete plates, and a vertical displacement-controlled test is initially performed until damage occurs at the contact, followed by imposing a controlled displacement on the upper particle in both the horizontal and vertical directions. In all tests, the contact unit normal and the contact surface location were defined as if the lower spherical has a plate-like geometry, dashed line in Figure 5, assuring that pure shear tests could be performed with a single VGCM-3D contact.

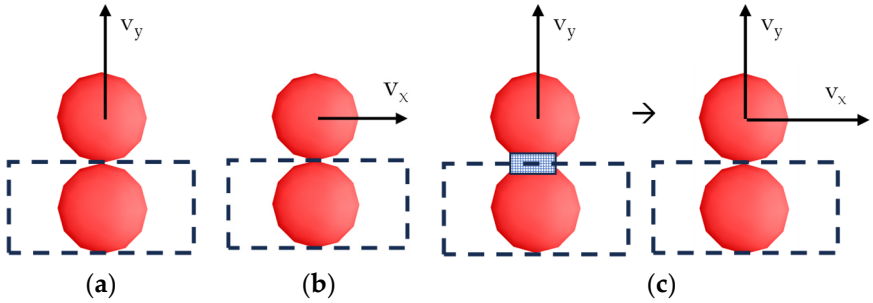

Figure 5. Single VGCM-3D contact test loading configurations: (**a**) tensile test (T); (**b**) shear test with an initial imposed axial force (S&A); and (**c**) mixed-mode experiment (HMM).

The adopted elastic and strength contact properties in the tensile tests (T), the shear tests with axial force (S&A), and the mixed-mode tests (HMM) are presented in Table 1. The adopted contact values closely resemble those adopted in [33], where the cohesive fracture constitutive contact model (CFM) is presented and validated.

Table 1. VGCM3D single-contact elastic and strength properties.

	$\overline{E}$ (GPa)	α	μ_c	$\sigma_{n.t}$ (MPa)	τ (MPa)	$G_{f.n}$ (N/mm)	$G_{f.s}$ (N/mm)	μ_{cr}	τ_Q (MPa)	μ_{cQ}
T	6.0	1.0	0.8	3.0	14.0	0.015 & 0.03	0.1	0.2	-	-
S&A [1]	112.5	1.0	0.8	3.0	4.5	0.025	0.06	0.2	45.0	0.04
HMM [2]	0.9	1.0	0.8	2.8	7.0	0.20	2.0	0.2	105.0	0.04

[1] $\sigma_c = 30.0$ MPa, $K_c = 0.1\ \overline{E}$ in the LSSB model. [2] $\sigma_c = 45.0$ MPa, $K_c = 0.1\ \overline{E}$ in the LSSB model.

Figure 6 shows the predicted tensile test stress–displacement curves for two different values of contact fracture energy in mode I. As shown, under tensile loading, the BL contact model is a bilinear approximation of the responses obtained with the LSSB and with the CFM contact models, in which the softening branch closely follows an exponential decay. Figure 6 also shows that in all adopted contact models, a higher fracture energy in mode I

leads to a more ductile response under tensile loading in all tests and that the predicted maximum strength is the input value (3 MPa).

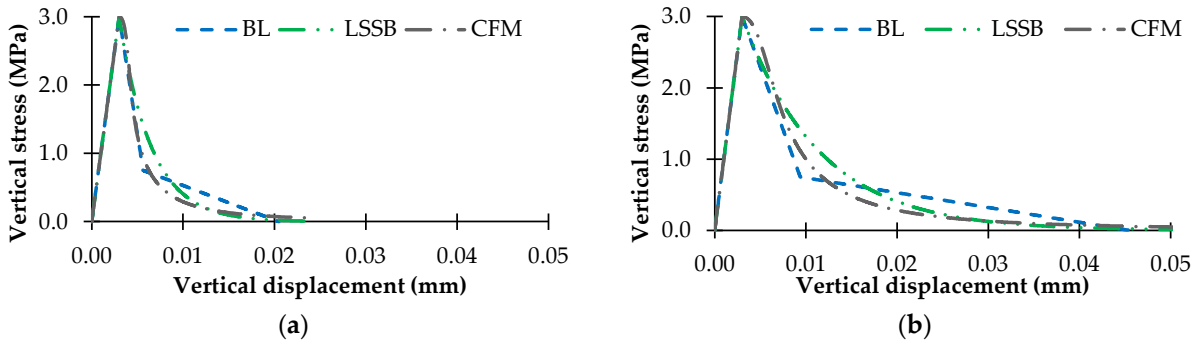

Figure 6. Tensile test (T)—stress vs. displacement for different values of $G_{f.n}$: (**a**) $G_{f.n}$ = 0.015 N/mm and (**b**) $G_{f.n}$ = 0.03 N/mm.

Figure 7 shows the predicted shear test stress–displacement curves for four distinct imposed axial stress values ($\sigma_v = 0.05$ MPa, $\sigma_v = 0.0$ MPa, $\sigma_v = -0.05$ MPa, and $\sigma_v = -6.0$ MPa). As shown, under shear loading, when compared with the tensile test, more noticeable differences in the predicted response obtained with each contact softening model can be identified. Under an imposed axial tensile stress, as shown in Figure 7a, the BL predicts a more ductile response than the LSSB and the CFM contact models' responses. Under a pure shear test, the contact models' predictions follow the trends previously observed in the tensile test, namely, the BL linear approximation to the more complex LSSB and CFM predicted responses, as shown in Figure 7b. Figure 7b also shows that under pure shear, the BL and the LSSB contact models predict similar responses, and the obtained maximum strength under pure shear is the initial input value (4.5 MPa), whereas in the CFM model, the maximum strength depends on the input contact strength value and the adopted initial frictional contact term. Figure 7c shows that under a low contact axial compression stress value, the responses predicted with the three contact models are similar. As shown in Figure 7d, for a higher initial compressive contact stress, the CFM model incorporates a degradation of the friction term, from the initial value of 0.8 to a residual value of 0.2. Figure 7d further demonstrates that the friction angle in the LSSB contact model is a variable internal to the model that is influenced by the ratio of normal to shear stiffness of the springs and the value of $\tan \omega_0$, as depicted in Figure 4a. Based on the data provided in Table 1, the internal frictional term for the LSSB contact model is calculated to be 0.97.

Figure 8 shows the predicted shear test stress–displacement curves in mixed mode for two different loading conditions ($\tan \theta = 30°$, $\tan \theta = 60°$). As shown, the single contact is initially cracked, adopting a displacement control procedure and at damage onset, a given vertical to horizontal displacement is imposed ($\tan \theta$). Figure 8 shows that the response predicted by the CFM closely matches the experimentally observed behaviour of a concrete plate [40]. This behaviour was expected given that the strength values listed in Table 1 are the same as those used in [33] to validate the CFM for the same experimental setup.

By considering dilatancy and a decrease in the frictional term with damage evolution, the CFM allows for a complex response to be predicted with a single contact that closely matches the response obtained with a concrete plate [40]. The BL and the LSSB contact models can be further calibrated to predict a response in closer agreement with the response obtained experimentally, namely, the peak values, but as shown, the response predicted with the BL contact model is much more brittle than the responses predicted with the LSSB and CFM contact models. Regardless, it is our point of view that in particle modelling, the complex macroscopic response should be an emergent behaviour from the overall material structure representation and material randomness and not due to a complex single-contact phenomenological constitutive law.

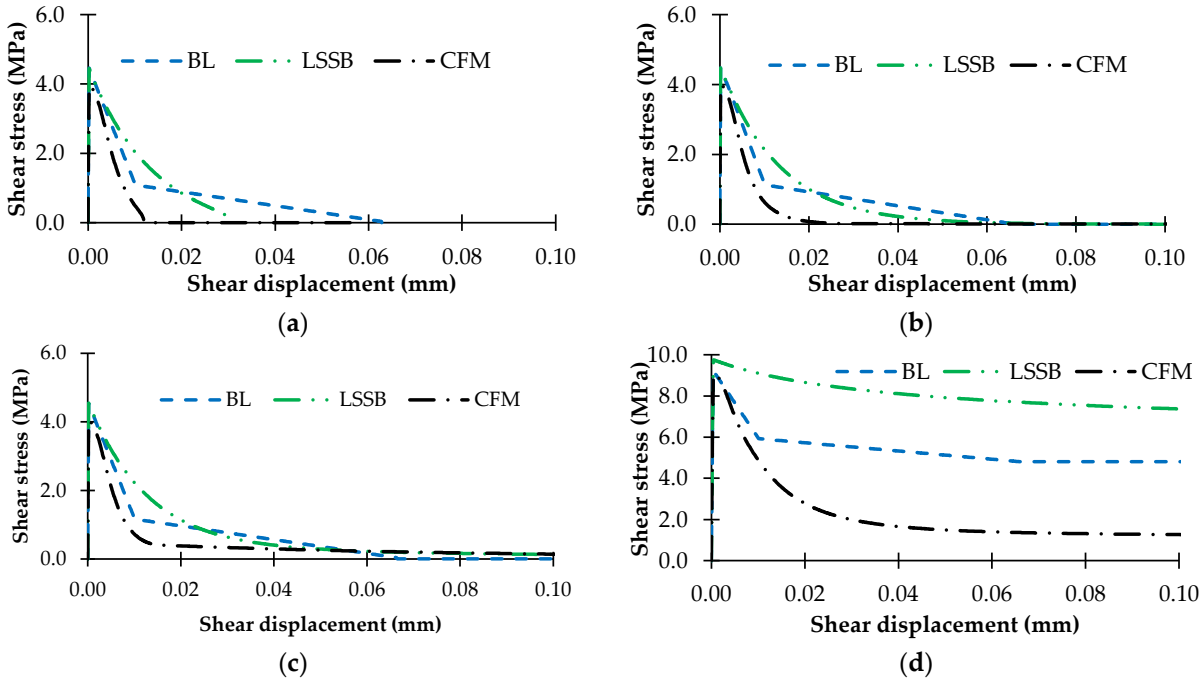

Figure 7. Shear test under constant axial stress (S&A)—stress vs. displacement for different values of imposed axial contact stress (σ_v): (**a**) $\sigma_v = 0.05$ MPa; (**b**) $\sigma_v = 0.0$ MPa; (**c**) $\sigma_v = -0.05$ MPa; and (**d**) $\sigma_v = -6.0$ MPa.

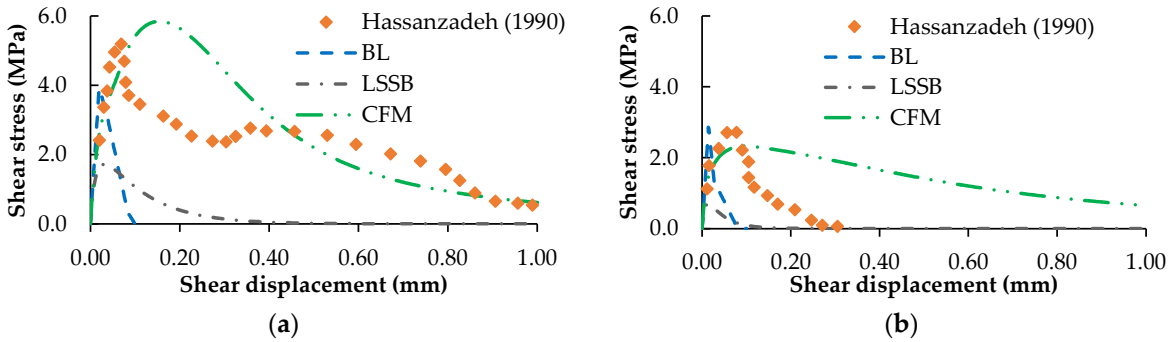

Figure 8. Mixed-mode experiment (HMM)—shear stress vs. shear displacement for different values of the vertical to shear displacement ratio ($\tan\theta = \frac{v_y}{v_x}$), including the experimental results Hassanzadeh (1990) adopted from [40]: (**a**) $\tan\theta = 30°$ and (**b**) $\tan\theta = 60°$.

3.3. Concrete Fracture Tests

3.3.1. Numerical Models

To assess the contact softening models under more complex geometries and loading conditions, uniaxial tensile tests, uniaxial compression tests, and biaxial tests were carried out using the geometries presented in Figure 9. As referred to in Section 2.4, the PMs under consideration directly incorporate an aggregate content spanning dimensions from 4.0 to 8.0 mm and from 8.0 to 16.0 mm, which represent 44% of the total volume within the aggregate size distribution [36]. Additionally, for mortar particle representation, a uniform distribution ranging between 4.0 and 5.0 mm in diameter and a porosity of 0.10 is adopted to adequately occupy the void space [6].

Due to computational restrictions, the biaxial tests were carried out in a $100 \times 100 \times 50$ mm^3 geometry, which is half of the size adopted experimentally, which is a $200 \times 200 \times 50$ mm^3 geometry [41]. The compression uniaxial tests assemblies have on average 1600 particles representing the aggregates and 12,200 particles representing the

mortar, corresponding to a total of 78,000 VGCM-3D contacts, which, in turn, correspond to a total of 478,500 local contacts, as shown in Figure 9.

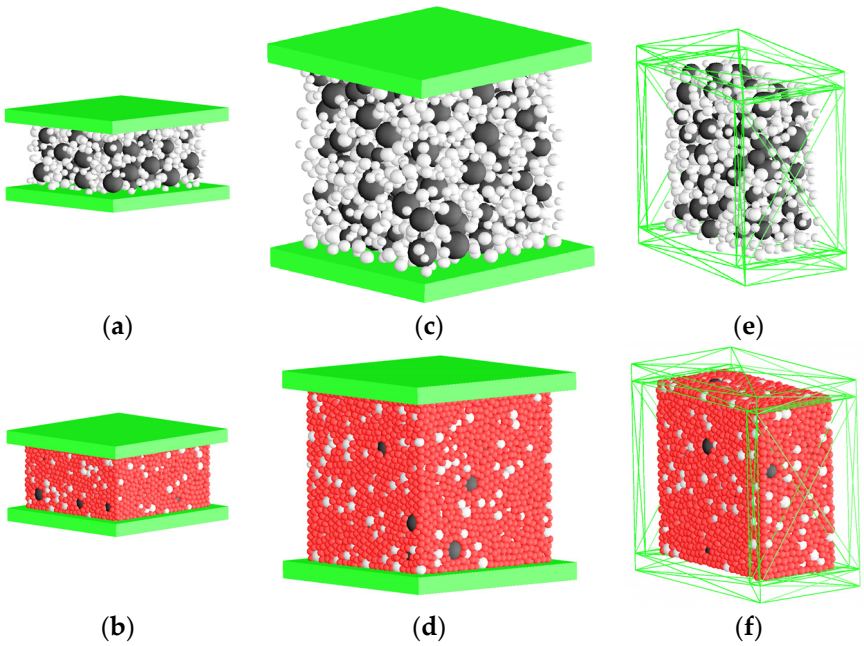

Figure 9. VGCM-3D concrete PMs: (**a**) tensile test (100 × 50 × 100 mm^3)—aggregate; (**b**) tensile test (100 × 50 × 100 mm^3)—aggregate + mortar; (**c**) compression test (100 × 100 × 100 mm^3)—aggregate; (**d**) compression test (100 × 100 × 100 mm^3)—aggregate + mortar; (**e**) biaxial test (100 × 100 × 50 mm^3)—aggregate; and (**f**) biaxial test (100 × 100 × 50 mm^3)—aggregate + mortar.

3.3.2. Best-Fit Properties

Two different approaches are adopted in 3D particle modelling of concrete as follows: (i) a uniform (U) approach that adopts similar contact properties across all contacts regardless of their origin and (ii) a heterogeneous approach that adopts different contact properties for the inter-particle contacts between the aggregate particles and the particles representing the mortar (A-M) and for the inter-particle contacts between the particles representing the mortar (M-M).

The adopted particle generation procedure presented in Section 2.4 also creates a small number of contacts between aggregate particles (A-A). In the heterogeneous approach (H), the contact properties adopted for the aggregate-to-aggregate contacts (A-A) are the same as the contact properties adopted for the aggregate-to-matrix (A-M) contacts.

Table 2 presents, for both approaches (U&H), the elastic contact properties that predict a numerical macroscopic Young's modulus of 32.0 GPa and a macroscopic Poisson coefficient of 0.12, similar to the concrete elastic properties adopted in [36].

Table 2. VGCM-3D contact elastic contact properties—uniform (U) versus heterogeneous (H) approach—concrete model best-fit properties.

Contact Type	U Approach		H Approach	
	$\overline{E}$ (GPa)	α	$\overline{E}$ (GPa)	α
A-A and A-M	54.1	0.17	81.45	0.20
M-M			27.15	0.20

Table 3 presents, for both approaches (U&H), the calibrated strength contact properties for the contact softening models that are assessed, which predict a numerical macroscopic uniaxial compressive strength (41.62 MPa) and a numerical macroscopic uniaxial tensile

strength (3.72 MPa) similar to the concrete strength properties adopted in [36]. In [36], it is shown that the numerical predictions of a 2D PM that considers a linear contact constitutive model and adopts a FEM discretization of the aggregates embedded in a cement paste matrix represent concrete uniaxial experimental behaviour well.

Table 3. VGCM-3D strength properties—concrete model best-fit properties.

(a) Uniform approach						
		$\sigma_{n.t}$ (**MPa**)	τ (**MPa**)	μ_c	$G_{f.n}$ (**N/mm**)	$G_{f.s}$ (**N/mm**)
BL (A-A, A-M, M-M)		6.33	20.25	0.2	0.0068	1.388
LSSB (A-A, A-M, M-M) [1]		5.95	12.65	-	0.0060	0.542
CFM (A-A, A-M, M-M) [2]		6.24	103.20	0.2	0.0066	36.064
(b) Heterogeneous approach						
		$\sigma_{n.t}$ (**MPa**)	τ (**MPa**)	μ_c	$G_{f.n}$ (**N/mm**)	$G_{f.s}$ (**N/mm**)
BL	A-A and M-M	10.20	35.80	0.2	0.0117	4.612
	A-M	5.10	17.90	0.2	0.0024	0.947
LSSB [1]	A-A and M-M	10.45	17.60	-	0.0123	0.592
	A-M	5.23	8.80	-	0.0025	0.122
CFM [2]	A-A and M-M	9.66	155.90	0.2	0.0105	46.466
	A-M	4.83	77.95	0.2	0.0022	9.548

[1] $\sigma_c = 450.0$ MPa, $K_c = 0.1\ \overline{E}$, $\mu_1 = 0.2$ in the LSSB model. [2] $\mu_{cr} = \mu_{cQ} = \mu_c$, $\tau_{cQ} = \tau$ in the CFM model.

In the literature, there are several automatic contact calibration approaches based on the design of experiment method (DOE), machine learning methods (ML), or evolutionary approaches (GA) [42–44] that do not rely on the user experience. In this work, a simple trial-and-error procedure that relies on the user experience with particle modelling was followed. Regarding the macroscopic elastic contact properties, the normal and the shear stiffness spring ratio (α) is the main parameter that controls the desired macroscopic Poisson's ratio, whereas the macroscopic Young's modulus is mostly controlled by the equivalent continuum material ($\overline{E}$) value [31,45]. Concerning the contact strength properties, the maximum contact tensile strength and the contact fracture energy in mode I are initially calibrated by adopting uniaxial tensile tests, and then the maximum contact cohesion strength, the contact frictional term, and the contact fracture energy in mode II are calibrated using uniaxial compressive tests.

With the BL and the LSSB contact models, the calibration procedure is more straightforward than with the CFM contact model, namely, under uniaxial compression. In the BL and LSSB contact models, an increase in the maximum contact cohesion strength is proportional to an increase in the macroscopic uniaxial compressive strength. It is important to point out that within a trial-and-error procedure, a uniform approach (U) calibration procedure is much easier to carry out than a heterogeneous approach (H) calibration procedure. In the heterogeneous approach, the adopted A-M to M-M elastic and strength contact properties ratio follows closely the values adopted in other PM studies [6,34].

In the best-fit calibration procedure that was carried out, it was decided to adopt the same contact frictional term in all contact models. In the LSSB contact model, a high uniaxial compressive contact strength of 450.0 MPa was considered for the stress boundary under high contact stress to not influence the numerical predictions, as shown in Figure 4a. It was also decided to adopt an associated formulation for the CFM contact model because, in the PMs, the non-associated macroscopic behaviour should be an emergent macroscopic property.

As shown in Table 3, the maximum contact tensile strength best-fit values, mostly related to the macroscopic uniaxial tensile strength, are very similar for all the assessed softening contact models. This can be explained because in a tensile test, damage occurs at contacts perpendicular to the load direction that carry small shear contact forces, and as

seen in the previous section, for a single contact, the response under pure tensile loading is very similar for all the assessed contact models.

The differences in the maximum contact cohesion term are more noticeable. The maximum contact cohesion stress is much higher in the CFM contact model than in the LSSB and BL contact models, as shown in Table 3. As referred to in Section 2.5.3, as the adopted contact frictional term of 0.2 is a low value for the CFM contact model, the maximum cohesion under pure shear is then much lower than the adopted maximum contact cohesion stress.

Figure 10 shows the axial stress–displacement numerical predictions for each contact softening model under uniaxial tensile and compression for both approaches (U&H). Similarly, Figure 11 presents the damage–displacement numerical predictions for the same set of tests and approaches. As shown in Figures 10 and 11, the three contact softening models under assessment can be calibrated to make them reproduce complex macroscopic behaviour in concrete under uniaxial tensile and compressive loading [36]. The predicted contact damage evolutions are also very similar among all softening-based contact models, especially under tensile loading, as shown in Figure 11.

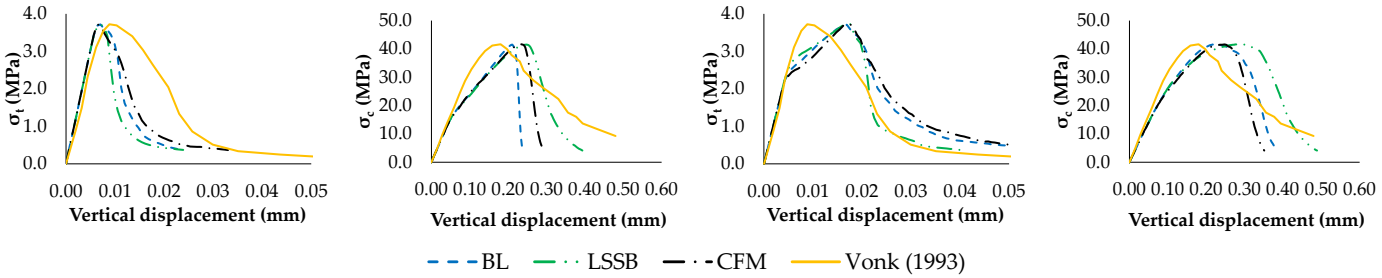

Figure 10. Concrete model best-fit properties—stress–displacement curves for the uniaxial tests, including Vonk (1993) adopted from [36]: (**a**) uniaxial tensile test—U approach; (**b**) uniaxial compression test—U approach; (**c**) uniaxial tensile test—H approach; and (**d**) uniaxial compression test—H approach.

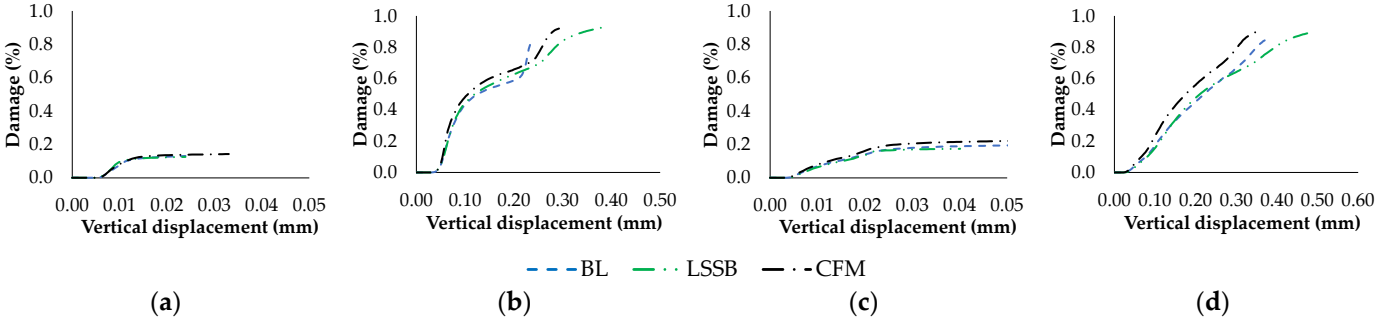

Figure 11. Concrete model best-fit properties—damage–displacement curves for the uniaxial tests: (**a**) uniaxial tensile test—U approach; (**b**) uniaxial compression test—U approach; (**c**) uniaxial tensile test—H approach; and (**d**) uniaxial compression test—H approach.

The contact softening-based models under assessment, after a previous calibration, have the following similarities:

- With a uniform (U) approach, the predicted numerical response under uniaxial tensile loading is slightly less ductile than the response predicted with the 2D PM flexible model that is known to represent concrete behaviour well [36]. Under a uniform approach (U), a softening contact model is fundamental in order for the PM not to predict a too brittle response, as shown in Figure 10a;

- In the uniform approach (U), at around 20.0 MPa compressive strength, there is a sudden change in stiffness: a two-slope stress–displacement response is clearly predicted with all contact models, as shown in Figure 10b. A similar behaviour has been found to occur in rock fracture tests using the BL contact model [31,45], and it was thought that it could be due to the simplified assumptions of the BL contact vectorial model. As will be shown, this anomalous two-slope behaviour can be mitigated in all contact modes by adopting a higher value of the normal-to-shear stiffness ratio;
- As expected, with a heterogeneous approach (H), the predicted uniaxial tensile and compression numerical responses are less brittle than the ones predicted with a uniform approach (U) and are in better agreement with the concrete experimental behaviour, as shown in Figure 11c,d;
- In the heterogeneous approach (H), at a uniaxial tensile loading of around 2.0 MPa applied stress, there is a clear loss of stiffness that is due to the damage that initially occurs at the A-M contacts that have lower contact strength properties. As will be shown, this predicted loss of stiffness can also be mitigated in all contact models by adopting a higher value of the normal-to-shear stiffness ratio.

Given the best-fit contact properties that were found through a trial-and-error procedure using uniaxial tests, numerical biaxial tests under loading control were also carried out. Figure 12 presents, for both approaches (U&H), the predicted biaxial failure envelopes for the best-fit contact strength properties. Also presented is the experimental envelope for a uniaxial compressive strength of 31 MPa [41] in the range of the concrete under assessment uniaxial compressive strength (41.62 MPa). As shown in Figure 12, all the assessed contact models under tensile/tensile and tensile/compression loading predict a failure envelope in close agreement with the known concrete behaviour [41]. Under compression/compression loading, all the contact models predict a much higher failure envelope than that observed experimentally in concrete.

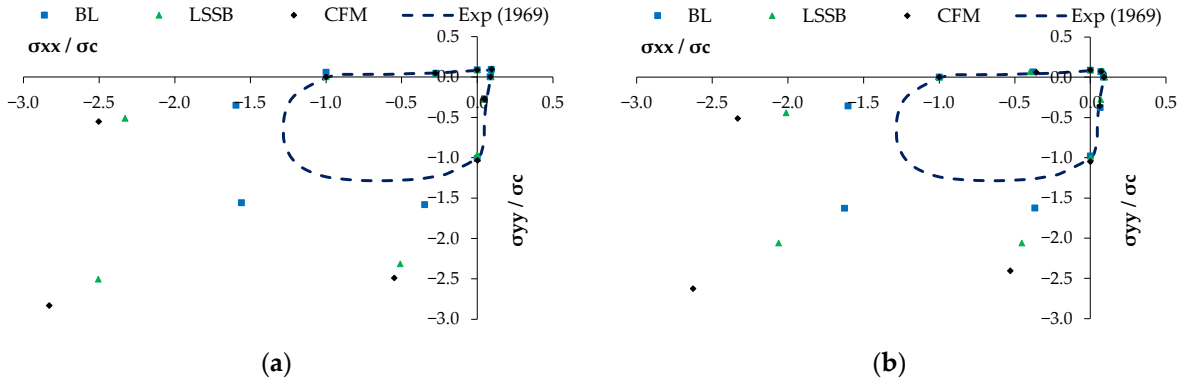

Figure 12. Concrete model best-fit properties—biaxial failure envelope including experimental envelope for $\sigma_c \approx 31$ MPa, Exp (1969) adopted from [41]: (**a**) U approach and (**b**) H approach.

In both approaches (U&H), the BL contact model predicts the best agreement in compression/compression loading, and the CFM contact model is the contact model whose predictions are further away from the known concrete experimental behaviour. The results obtained clearly show that a 3D PM particle model, based on a VGCM-3D contact model, following a Laguerre–Voronoi generation to set the inter-particle contacts and contact area, predicts a higher failure envelope under biaxial compression if the normal-to-shear stiffness ratio is set to predict the correct macroscopic Poisson's ratio.

In terms of computational costs, the BL contact model stands out as the most efficient. The LSSB contact model, compared with the BL contact model, has an associated computational cost that is 50% higher and the CFM contact model has an associated computational cost that is 15% higher. The computational costs within a 3D PM are of paramount

importance, particularly if larger structures are modelled or if more complex automatic calibration schemes are adopted that require a significant number of simulations.

In the numerical examples that were carried out, including the ones presented in the following sections, no convergence issues were identified when adopting the CFM contact model. This is most likely due to the fact that an explicit procedure was adopted that limits the contact force increment in each time step (small time steps or scaled masses). No solution issues were observed with the BL and LSSB contact models, both of which rely on the application of analytical expressions.

3.3.3. Normal-to-Shear Stiffness Ratio (α) of 0.50

The LSSB contact model that was proposed for a similar 3D PM, which just considers coarse aggregate particles and sets the contacts given a Delaunay triangulation, adopts a normal-to-stiffness spring ratio (α) of 0.25 [32]. The CFM contact model that was introduced within a FEM framework adopts an even higher normal-to-stiffness ratio (α) value of 1.0 [28]. Note that when adopting a flexible PM, Poisson's ratio is mainly associated with the adopted finite element Poisson's coefficient [34,36], and the normal and shear spring stiffnesses can be understood as being penalty terms.

As pointed out, within a PM framework, the α parameter should be chosen to ensure that the desired macroscopic Poisson's ratio is predicted, and as shown for the adopted 3D PM based on Laguerre–Voronoi tessellation, values of α much lower than the ones adopted in other PMs may be required (Table 2).

To assess the relevance of the α parameter, the same numerical tests in Section 3.3.2 were carried out with the best-fit contact strength properties presented in Table 3 and with the equivalent continuum material ($\overline{E}$) values presented in Table 2, but with a normal-to-stiffness ratio (α) of 0.50. With the newly adopted elastic contact properties, a macroscopic Young's modulus of 42.0 GPa and a macroscopic Poisson coefficient of 0.11 are predicted with a uniform approach (U), and a macroscopic Young's modulus of 41.6 GPa and a macroscopic Poisson coefficient of 0.12 are predicted with a heterogeneous approach (H). When adopting an α parameter value of 0.50, similar trends were identified in the numerical tests that were carried out with the different contact softening-based models:

- In both approaches (U&H) a higher value of α leads to higher values of tensile and compression strength and to lower ductility after the peak strength is reached, as shown in Figure 13a–d;
- Noticeable under tensile loading, the increase in peak strength is very similar in all contact models, as shown in Figure 13a,c. Interestingly, under uniaxial compression, the increase in the peak strength is less noticeable with a BL contact model than with the LSSB and CFM contact models;
- In the uniform approach (U), an anomalous two-slope stress–displacement response is no longer predicted under uniaxial compression, as shown in Figure 13b. In the heterogeneous approach (H), a loss of stiffness in the tensile test is mitigated when compared with the response predicted with a lower α value, as shown in Figures 10c and 13c;
- Under biaxial compression, as shown in Figure 14, the 3D PM predicted responses are closer to the observed concrete behaviour than the responses predicted with a lower α value, as shown in Figure 12.

Under biaxial compression, the 3D PM response adopting a BL contact model is in close agreement with the behaviour observed experimentally for concrete in both approaches (U&H). Like in the previous example, the CFM contact model predicts a larger failure envelope under biaxial compression. The results presented show that with an increase in the normal to stiffness ratio, all softening-based contact models predict failure envelopes under biaxial compression loading closer to those observed in concrete. Note that this improvement in the predicted macroscopic biaxial response is due to a worst macroscopic Poisson's coefficient prediction.

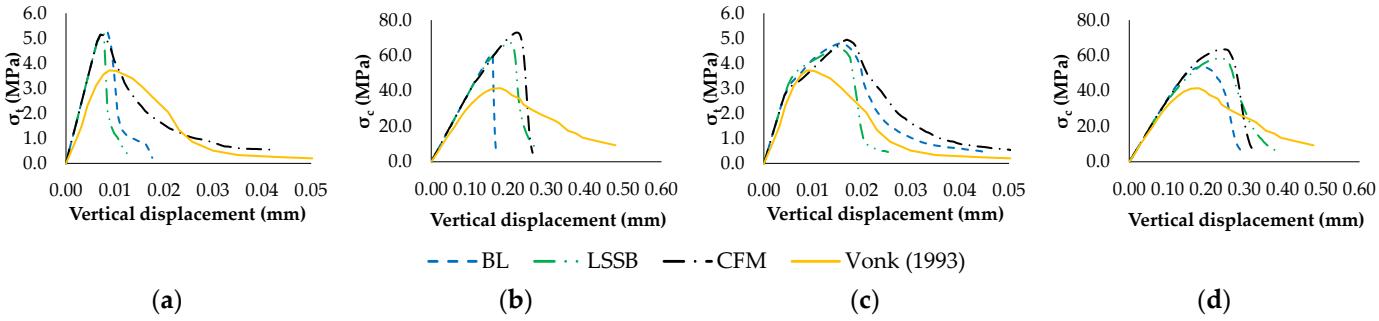

Figure 13. α parameter influence—stress–displacement curves for the uniaxial tests, including Vonk (1993) adopted from [36]: (**a**) uniaxial tensile test—U approach; (**b**) uniaxial compression test—U approach; (**c**) uniaxial tensile test—H approach); and (**d**) uniaxial compression test—H approach.

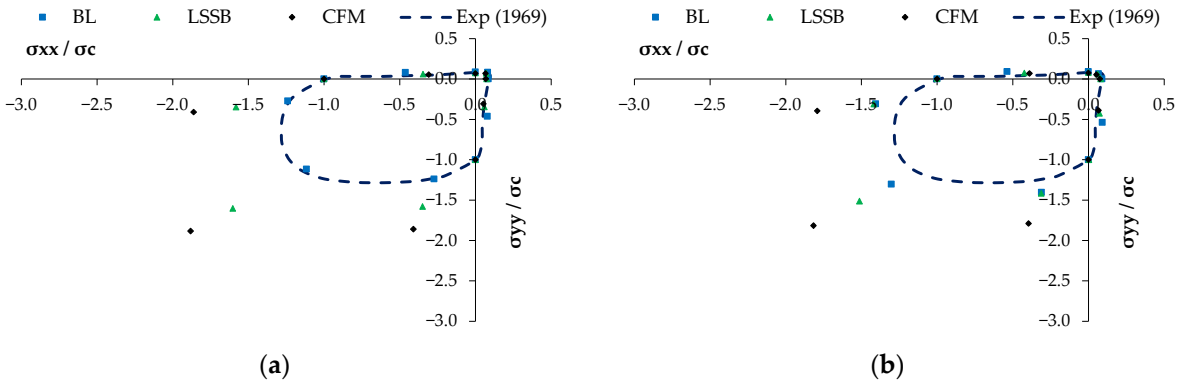

Figure 14. α parameter influence—biaxial failure envelope including the experimental envelope for $\sigma_c \approx 31$ MPa, Exp (1969) adopted from [41]: (**a**) U approach and (**b**) H approach.

3.3.4. A 30% Reduction in the PM Total Number of Contacts

As shown in the previous section, an increase in the normal-to-stiffness ratio value (α) leads to a better agreement with known concrete biaxial behaviour when compared with the response predicted with a lower α value that is required so that a 3D PM based on a Laguerre–Voronoi generation procedure predicts a correct macroscopic Poisson's ratio, especially under a uniform approach (U).

To predict a correct macroscopic Poisson's ratio in the order of 0.20 with a higher α parameter, one possibility is to transform some of the VGCM-3D contacts present in the PM into cohesionless contacts, which are contacts that are no longer able to carry tensile forces. For example, all the VGCM-3D contacts that have a contact area below a given threshold can be transformed into cohesionless contacts. Table 4 presents the best-fit calibrated elastic contact properties when the VGCM-3D contacts below a contact area of 6.0×10^{-6} m^2 are transformed into cohesionless contacts. A 30% reduction in the total number of VGCM-3D contacts is obtained. The smaller contact areas correspond in general to interacting particles that are further apart than the average inter-particle distance. Table 4 presents, for both approaches (U&H), the elastic contact properties that predict a numerical macroscopic Young's modulus of 32.0 GPa and a macroscopic Poisson coefficient of 0.20 [36]. The contact strength properties presented in Table 3 for the full particle assemblies were adopted.

If the number of contacts present in the PM that are able to carry tensile forces is initially reduced, similar trends are identified with the different contact softening-based models as follows:

- In both approaches, the reduction in the uniaxial tensile strength is more noticeable than the reduction in the uniaxial compressive strength, as shown in Figure 15a–d;

- The predicted stress–displacement responses have a better agreement with uniaxial concrete behaviour when compared with the predicted curves when all contacts are adopted, as shown in Figure 10;
- In the uniform approach (U), as shown in Figure 15b, the predicted two-slope stress–displacement response is much smoother than the one predicted in Section 3.3.2 (Figure 10b). In the heterogeneous approach (H), as shown in Figure 15c, a loss of stiffness in the tensile test is almost mitigated when compared with the response predicted in Section 3.3.2 (Figure 10c);
- Under biaxial compression loading, as shown in Figure 16, when compared with the response predicted in Section 3.3.2, the 3D PM predicted responses with a reduction in the total number of contacts are closer to that observed in concrete. Under a heterogeneous approach (H), the response predicted with the LSSB contact model has an excellent agreement with the response predicted with the BL contact model. The CFM contact model predictions are still too far away from the known concrete behaviour under biaxial compression.

Table 4. Contact reduction—VGCM3-D contact elastic contact properties—uniform (U) versus heterogeneous (H) approach—contact reduction.

Contact Type	(U) Approach		(H) Approach	
	$\overline{E}$ (GPa)	α	$\overline{E}$ (GPa)	α
A-A and A-M	51.5	0.25	75.90	0.30
M-M			25.20	0.30

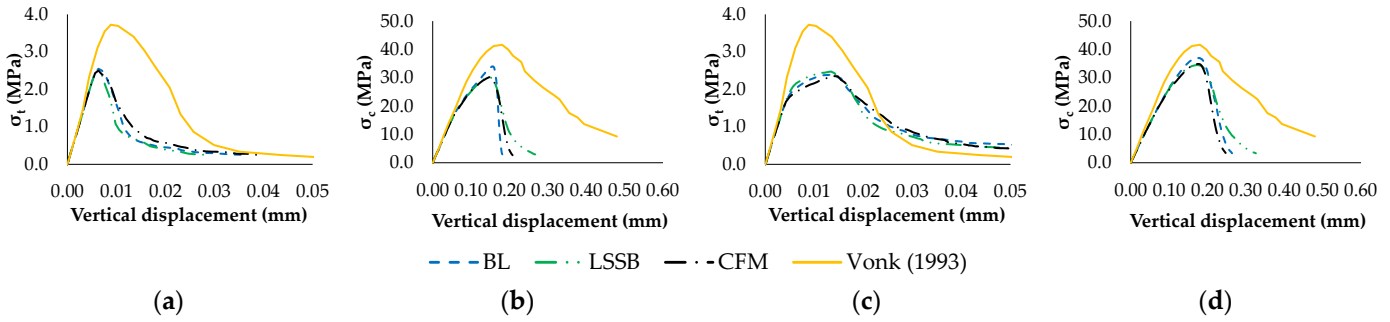

Figure 15. Contact reduction—stress–displacement curves for the uniaxial tests, including Vonk (1993) adopted from [36]: (**a**) uniaxial tensile test—U approach; (**b**) uniaxial compression test—U approach; (**c**) uniaxial tensile test—H approach); and (**d**) uniaxial compression test—H approach.

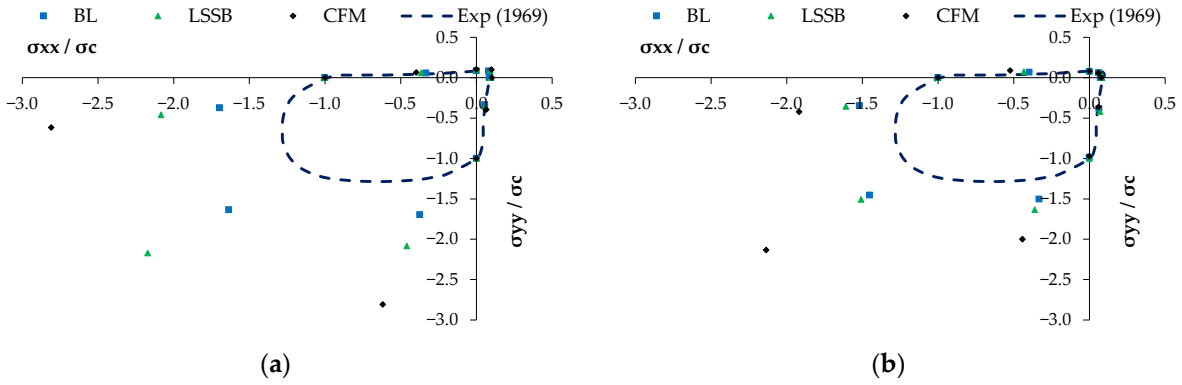

Figure 16. Contact reduction-biaxial failure envelope for best-fit contact strength properties including the experimental envelope for $\sigma_c \approx 31$ MPa, Exp (1969) adopted from [41]: (**a**) U approach and (**b**) H approach.

In both approaches (U&H), and for the LSSB contact model and the CFM contact model, the decrease in the uniaxial tensile strength (≈32%) is in the same order of magnitude as the decrease in the predicted uniaxial compression strength (≈28%). With a BL contact model, the decrease in the predicted uniaxial compressive strength is slightly lower (≈28%) than the decrease in the uniaxial tensile strength, which is in the same order as the decrease obtained with the other softening contact models.

With a reduction in the number of working contacts by setting cohesionless contacts given a certain contact area threshold, a better agreement with known concrete behaviour is obtained with all contact softening-based models. The better agreement is more noticeable with the BL contact model and with the LSSB contact model following a heterogeneous approach (H). Note that with an initial contact reduction, the proper macroscopic elastic behaviour is predicted with an increase in the normal-to-shear ratio.

3.3.5. Maximum Compressive Contact Strength of 60.0 MPa

The LSSB contact model also includes a stress–strain boundary for higher compression contact stresses, which was not considered in the previous calculations given that a high contact maximum strength (450 MPa) was adopted, see Table 3 and Section 2.5.2. In this section, the LSSB contact model was calibrated by adopting a maximum compressive contact stress of 60.0 MPa (LSSB-Y). The BL contact model was also extended to include a yield plateau (BL-Y) in the normal direction under compression. For the BL-Y contact model, the contact strength properties were calibrated using a yield compressive contact stress of 60.0 MPa. Compression cap models have also been proposed as an extension of the CFM contact model [46] and within the DEM framework [14,47] for masonry analysis. A CFM compression cap extension has not been implemented in the VGCM-3 contact model. For this reason, the effect of adopting a maximum compressive contact strength was not evaluated for the CFM contact model. To ease the calibration procedure, the influence of the maximum contact compressive strength was only assessed for a uniform (U) approach.

Table 5 presents the best-fit properties for the BL-Y and LSSB-Y contact models. As shown, when compared with the values presented in Table 3, for the BL contact model, the maximum cohesion stress value is higher when a compressive strength yield plateau is adopted. For the LSSB contact model, which adopts a more complex stress boundary for high axial stresses, both the tensile and the shear maximum contact strengths needed to be increased when a contact compressive strength of 60.0 MPa was considered.

Table 5. Compressive contact strength influence on VGCM3D strength properties—uniform (U) approach.

	$\sigma_{n.t}$ **(MPa)**	τ **(MPa)**	μ_c	$G_{f.n}$ **(N/mm)**	$G_{f.s}$ **(N/mm)**
BL-Y (A-A, A-M, M-M) [1]	6.33	24.40	0.2	0.0068	1.388
LSSB-Y (A-A, A-M, M-M) [2]	6.15	12.65	-	0.0064	0.894

[1] $\sigma_c = 60.0\ MPa$ yielding value under compression in the BL model. [2] $\sigma_c = 60.0\ MPa$, $K_c = 0.1\ \overline{E}$, $\mu_1 = 0.2$ in the LSSB model.

Figure 17 presents the predicted stress displacement curves including the numerical behaviour predicted in Section 3.3.2. As shown, under uniaxial tensile loading, the predicted response is very similar in both contact models (Figure 17a,c). Under uniaxial compression, as shown in Figure 17b,d, the response predicted with the LSSB-Y contact model is less brittle than the response predicted when a high maximum compressive strength is adopted. With the BL contact model, the consideration of a yield compressive contact strength does not have much influence on the post-peak region, and the BL and the BL-Y predicted responses are similar, as shown in Figure 17b.

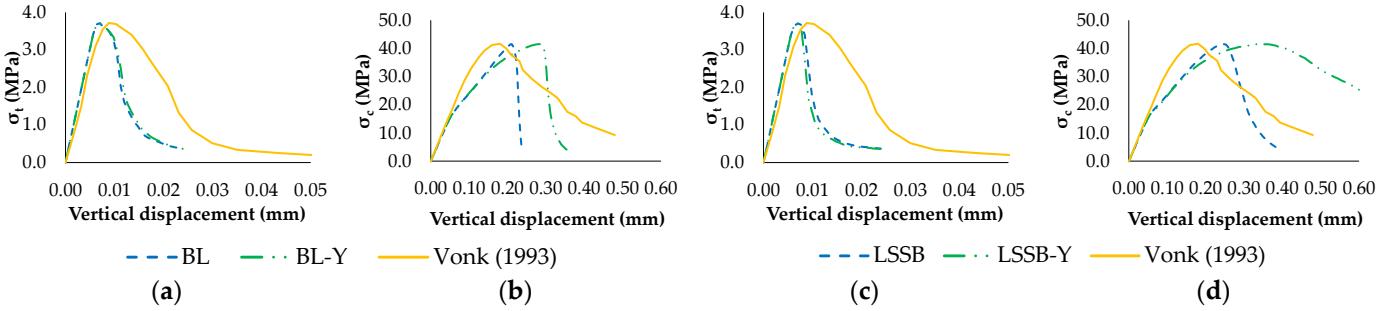

Figure 17. Maximum compressive contact strength—stress–displacement curves for the uniaxial tests, including Vonk (1993) adopted from [36]: (**a**) uniaxial tensile test—U approach; (**b**) uniaxial compression test—U approach; (**c**) uniaxial tensile test—H approach; and (**d**) uniaxial compression test—H approach.

Figure 18 presents the predicted biaxial failure envelopes when a maximum compressive contact strength is adopted. As expected, a maximum contact compressive strength of 60.0 MPa leads, in both the BL and LSSB contact models, to failure envelopes under biaxial compressive stress closer to those observed in concrete. The BL-Y contact model with a yield compressive value of around 150% of the macroscopic concrete compressive strength value leads to a very good agreement with the concrete experimental response under biaxial loading, as shown in Figure 18a.

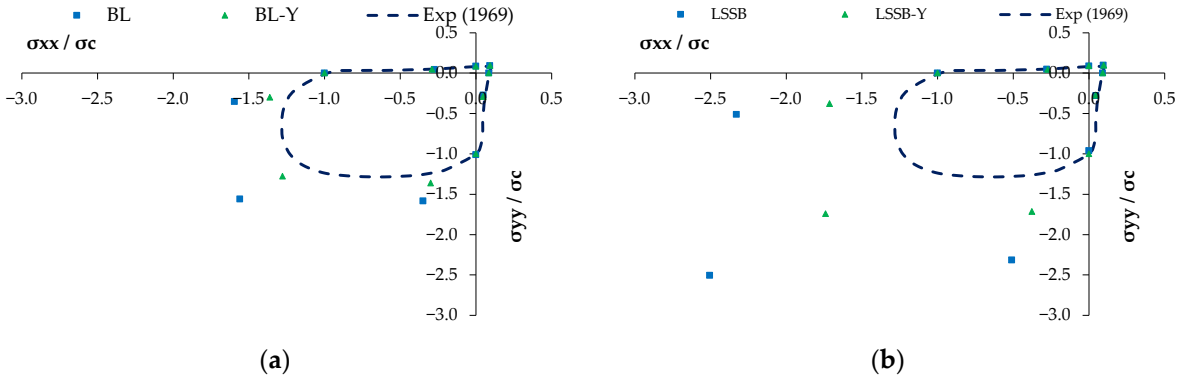

Figure 18. Maximum compressive contact strength—-biaxial failure envelope including the experimental envelope for $\sigma_c \approx 31$ MPa, Exp (1969) adopted from [41]: (**a**) BL contact model and (**b**) LSSB contact model.

3.3.6. Single-Point Contact Model (PCM)

It has been shown that a contact model that allows moment transmission increases the compression-to-tensile ratio for the same set of parameters [31,45]. In [7], it is mentioned that with a similar spherical PM representing concrete that does not take into account moment transmission, a compressive-to-tensile strength ratio of 8 is only possible following a uniform approach if the particle rotations are prevented; otherwise, only a ratio of 3 to 4 is obtained.

In this section, the VGCM-3D with a single local contact point is evaluated to assess the influence that the moment transmission has on the contact softening models. The concrete that was modelled had a compressive-to-tensile strength ratio of around 11.20, and with a uniform approach (U), it was not possible to find a set of contact strength parameters for all contact models that had a similar compressive-to-tensile strength ratio, even when higher maximum cohesion stress values and high contact frictional terms were adopted. Within a uniform approach (U), the maximum predicted numerical compressive tensile strength ratio with a PCM was ≈7.2 for the BL contact model, ≈6.5 for the LSSB contact model, and ≈8.0 for the CFM contact model.

Table 6 presents the best-fit strength properties for the PMs with a PCM for the heterogeneous approach (H). As shown, when adopting a single contact point, higher values of maximum cohesion stress values needed to be adopted when compared with values adopted when moment transmission is considered. For the CFM, it was also necessary to increase the contact frictional term to predict the desired compressive-to-tensile strength ratio. The best fit maximum tensile strength values, as shown in Table 6, are of the same order as the values adopted when moment transmission is considered, as shown in Table 3.

Table 6. PCM—VGCM3-D strength properties—concrete model best-fit properties—heterogeneous (H) approach.

		$\sigma_{n.t}$ (MPa)	τ (MPa)	μ_c	$G_{f.n}$ (N/mm)	$G_{f.s}$ (N/mm)
BL	A-A and M-M	10.12	80.00	0.2	0.0114	22.797
	AM	5.06	40.00	0.2	0.0023	4.696
LSSB [1]	A-A and M-M	10.52	70.00	-	0.0123	9.273
	AM	5.26	35.00	-	0.0025	1.910
CFM [2]	A-A and M-M	9.56	460.00	0.5	0.0101	40.420
	AM	4.78	230.00	0.5	0.0021	8.248

[1] $\sigma_c = 450.0$ MPa, $K_c = 0.1\ \overline{E}$, $\mu_1 = 0.2$ in the LSSB model. [2] $\mu_{cr} = \mu_{cQ} = \mu_c$, $\tau_{cQ} = \tau$ in the CFM model.

Figure 19 shows, for the PCM and for each contact softening model, the axial stress–displacement numerical predictions under uniaxial tensile and compression for the heterogeneous (H) approach. Under uniaxial tensile loading, the responses predicted with a PCM, as shown in Figure 16a, and with a contact model that allows moment transmission, as shown in Figure 10c, are very similar. Under uniaxial compressive loading, the responses predicted with a PCM, as shown in Figure 19b, have, for all contact models, a much more brittle post-peak behaviour than the responses predicted with a contact model that allows moment transmission, as shown in Figure 10d.

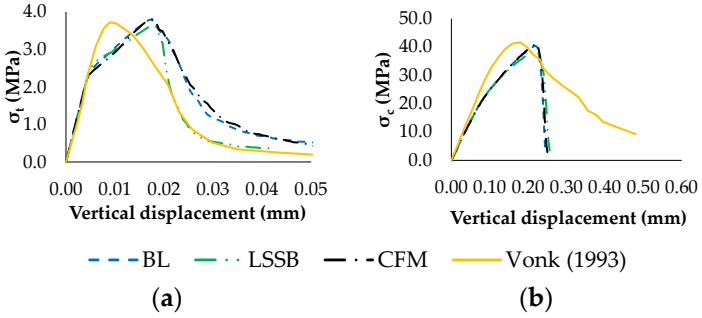

Figure 19. PCM—stress–displacement curves for the uniaxial tests, including Vonk (1993) adopted from [36]: (**a**) uniaxial tensile test—H approach and (**b**) uniaxial compression test—H approach.

Figure 20 presents, for all the assessed contact models, the predicted biaxial failure envelope. Also presented as a dashed line are the predictions obtained with a contact model that considers moment transmission; see Section 3.3.2. As shown for the BL contact model, the failure envelope under biaxial compression is of the same order as the failure envelope predicted with a contact model that allows moment transmission, whereas for the LSSB contact model and for the CFM contact model, the predicted failure envelopes under biaxial compression are lower than the failure envelopes predicted with a contact model that allows moment transmission. Noticeably, with a PCM, the biaxial failure envelopes predicted with the three contact softening models under analysis are in closer agreement than the biaxial failure envelope predicted when moment transmission is considered.

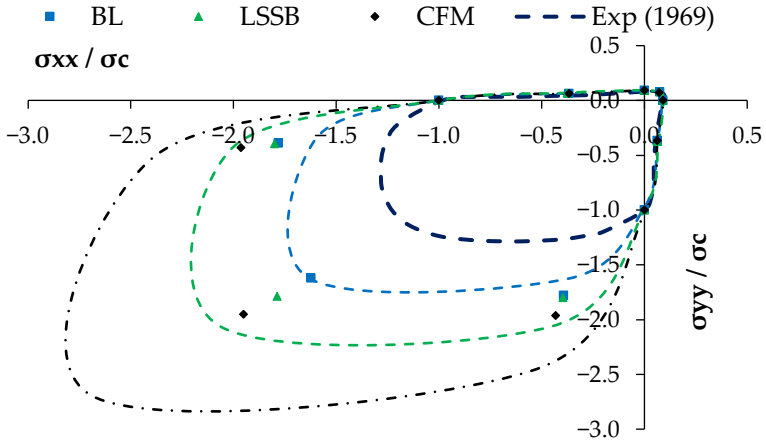

Figure 20. PCM—biaxial failure envelope for best-fit contact strength properties including the experimental envelope for $\sigma_c \approx 31$ MPa, Exp (1969) adopted from [41]—heterogeneous (H) approach.

Figure 21 presents, for all the assessed contact models, the best-fit predicted biaxial failure envelopes obtained with a PCM for both approaches when a normal-to-shear stiffness ratio of 0.50 is adopted. Under this assumption, the PMs predict a failure biaxial envelope in close agreement with that observed in concrete, especially for the BL and LSSB contact models. It can be highlighted that with a PCM, a 60% computational time reduction is obtained when compared with a 3D PM that considers moment transmission. However, as pointed out, with a PCM, a uniform approach cannot be adopted if a compression-to-tensile ratio higher than 8.0 is required.

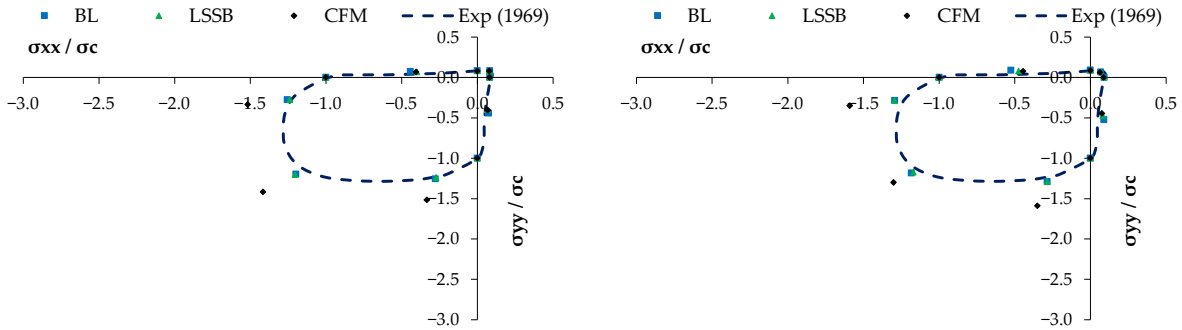

Figure 21. PCM ($\alpha = 0.5$)—biaxial failure envelope including the experimental envelope for $\sigma_c \approx 31$ MPa, Exp (1969) adopted from [41]: (**a**) uniform (U) approach and (**b**) heterogeneous (H) approach.

3.3.7. PM Refinement

To evaluate the performance of the contact softening models with a more detailed discretization, an aggregate content featuring sizes from 2.0 to 4.0 mm, 4.0 to 8.0 mm, and 8.0 to 16.0 mm, which makes up to 58% of the total aggregate volume distribution, is considered [36]. Additionally, for the mortar representation, a uniform particle size distribution ranging from 2.5 to 3.0 mm and a porosity of 0.1 is selected to effectively fill the void space [6].

In the refined PMs, the compression uniaxial test assemblies have on average 10,100 particles representing the aggregates and 39,000 particles representing the mortar, corresponding to a total of 308,000 VGCM-3D contacts, which, in turn, correspond to a total of 1,850,200 local contacts. Compared with the coarser model adopted in the previous examples, the refined model is much more computationally demanding. Within a particle modelling approach, the particle content should be as close as possible to the real concrete

aggregate/mortar content; however, due to computational restrictions, there must be a compromise on the degree of refinement, especially in 3D PMs.

Table 7 presents the best-fit contact elastic properties and Table 8 presents the best-fit strength properties for the more refined PMs for both approaches (U&H). As shown, given that a PM based on a Laguerre–Voronoi tessellation of the particles' gravity centres assures a certain degree of regularization, contact area, and contact length, the best-fit parameters of a refined PM are closer to the best-fit parameters of a coarser PM; see Table 2 versus Tables 3 and 7 versus Table 8. This type of behaviour is not possible to obtain with a PM that sets the contact areas as a function of the particles' interacting radius [8,10].

Table 7. Three-dimensional PM refinement—VGCM-3D contact elastic contact properties—uniform (U) versus heterogeneous (H) approach.

Contact Type	Uniform Approach		Heterogeneous Approach	
	$\overline{E}$ (GPa)	α	$\overline{E}$ (GPa)	α
A-A and A-M	54.1	0.17	71.80	0.20
M-M			23.90	0.20

Table 8. VGCM3D strength properties—concrete model best-fit properties—refined PMs.

(a) Uniform (U) approach						
		$\sigma_{n.t}$ (MPa)	τ (MPa)	μ_c	$G_{f.n}$ (N/mm)	$G_{f.s}$ (N/mm)
BL (A-A, A-M, M-M)		6.30	20.13	0.2	0.0043	0.946
LSSB (A-A, A-M, M-M) [1]		6.00	13.55	-	0.0039	0.397
CFM(A-A, A-M, M-M) [2]		6.24	105.80	0.2	0.0042	24.418
(b) Heterogeneous (H) approach						
		$\sigma_{n.t}$ (MPa)	τ (MPa)	μ_c	$G_{f.n}$ (N/mm)	$G_{f.s}$ (N/mm)
BL	A-A and M-M	11.50	33.34	0.2	0.0108	2.895
	A-M	5.75	16.67	0.2	0.0022	0.602
LSSB [1]	A-A and M-M	11.66	19.02	-	0.0111	0.500
	A-M	5.83	9.51	-	0.0023	0.104
CFM [2]	A-A and M-M	11.10	139.50	0.2	0.0100	26.922
	A-M	5.55	69.75	0.2	0.0021	5.596

[1] $\sigma_c = 450.0$ MPa, $K_c = 0.1\ \overline{E}$, $\mu_1 = 0.2$ in the LSSB model. [2] $\mu_{cr} = \mu_{cQ} = \mu_c$, $\tau_{cQ} = \tau$ in the CFM model.

Figure 22 shows the axial stress–displacement numerical predictions for each contact softening model under uniaxial tensile and compression for both modelling approaches (U&H). As shown, for all contact models, the refined PM numerical predictions, which have a much higher associated computational cost, are closer to the coarser PM predictions; see Figures 10 and 22.

Figure 23 presents the predicted biaxial failure envelopes for all the assessed contact models. Also presented as a dashed line are the predictions obtained with a coarser model. In a uniform approach (U), the refined PM calibrated predictions are in close agreement with the predictions obtained with the coarser PM, whereas in the heterogeneous approach (H), the refined PM predictions are closer to the observed concrete behaviour under biaxial loading. Noticeably, the differences are more pronounced with a CFM contact model.

The results presented show that for all softening-based contact models and for all modelling approaches, it is possible to carry out a two-step calibration procedure that greatly reduces the required computational times. First, the best-fit parameters can be found using a coarser assembly with reduced computational costs and then a localized refinement can be carried out with the refined PMs.

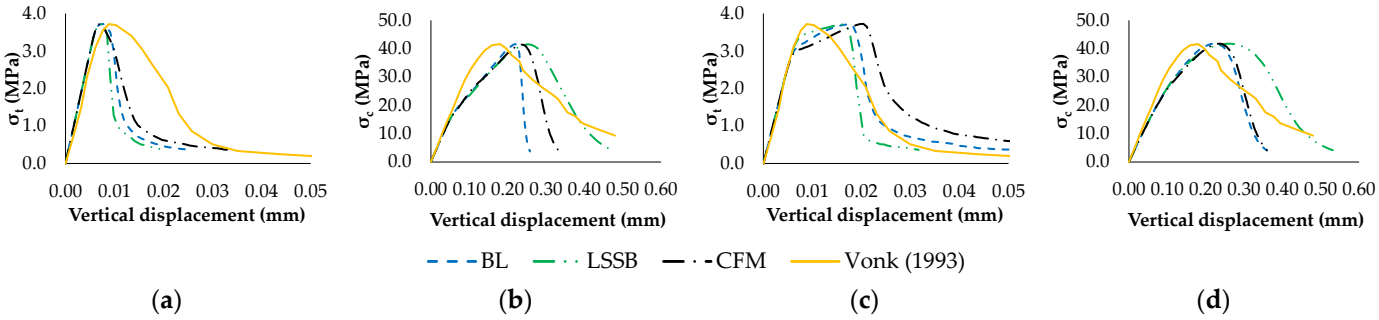

Figure 22. Three-dimensional PM refinement—stress–displacement curves for the uniaxial tests, including Vonk (1993) adopted from [36]: (**a**) uniaxial tensile test—U approach; (**b**) uniaxial compression test—U approach; (**c**) uniaxial tensile test—H approach; and (**d**) uniaxial compression test—H approach.

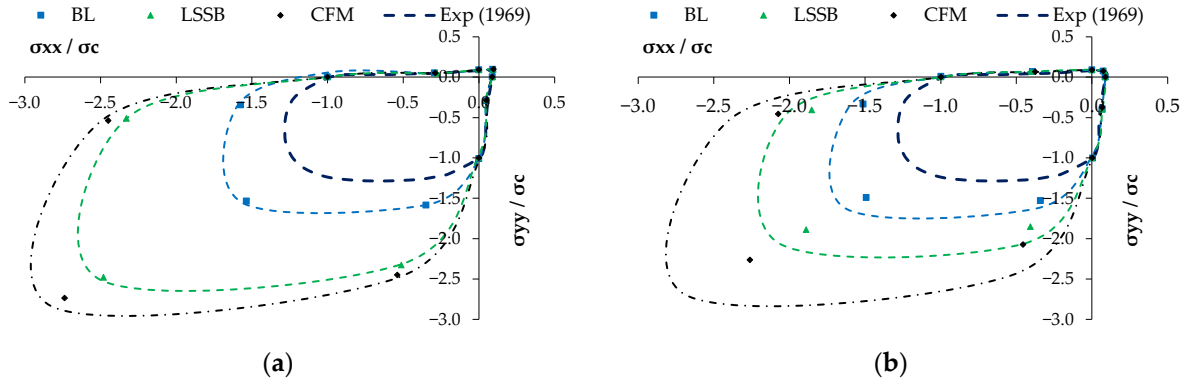

Figure 23. Three-dimensional PM refinement—biaxial failure envelope including the experimental envelope for $\sigma_c \approx 31$ MPa, Exp (1969) adopted from [41]: (**a**) uniform approach and (**b**) heterogeneous approach.

4. Discussion and Conclusions

Given that some limitations have been identified when using a PM that adopts a BL contact model, namely, a clear two-slope curve is predicted under uniaxial compression for hard rock, BL contact model predictions are compared with those obtained using more complex contact models for different application examples adopting a 3D rigid PM.

4.1. Single VGCM-3D Contact

For a single contact point under tensile loading, the contact softening models' response is very similar. Under pure shear loading, there are some differences in the numerical predictions, especially between the CFM contact model and the other contact models given that in the CFM contact model, the maximum shear cohesion strength input value does not match the maximum predicted shear strength, particularly for lower contact frictional values. For the shear tests under constant axial force, more noticeable differences in the responses are identified as follows: (i) in the LSSB contact model, the contact frictional term is an internal variable and (ii) the CFM contact model can include a deterioration of the frictional term with damage evolution. For a complex mixed-mode test under displacement control, the difference in the predicted responses is even more evident. The response predicted with a single CFM contact model under mixed mode can be quite complex as the model also allows non-associated plastic flow.

4.2. Uniaxial and Biaxial Behaviour for Best-Fit Properties

Uniaxial tensile and uniaxial compression tests and biaxial tests of 3D PMs representing concrete were also carried out, following a uniform and heterogeneous approach. As shown in both approaches, it is possible to calibrate the 3D PM contact strength properties in

order for each softening-based contact model to predict the known experimental behaviour of concrete under uniaxial tensile and uniaxial compressive loading. The maximum contact tensile strength values, mostly related to the macroscopic uniaxial tensile strength, are very similar for all the assessed softening contact models. The differences in the maximum contact cohesion terms are more noticeable, and the maximum contact cohesion stress is much higher in the CFM contact model than in the LSSB and BL contact models, but despite the differences in value, the contact models do lead to similar macroscopic responses.

The contact softening-based contact models under assessment after a previous calibration have some similarities in the predicted behaviour under uniaxial loading as follows: (i) in the uniform approach (U), a two-slope stress–displacement response is clearly predicted with all contact models at around a 20.0 MPa compressive strength and (ii) in the heterogeneous approach (H), there is a clear loss of stiffness at a uniaxial tensile loading at around 2.0 MPa of applied stress. Previously, it was thought that these anomalies could be due to the vectorial nature of the BL contact model.

For the best-fit contact strength parameters, all the assessed contact models under tensile/tensile and under tensile/compression loading predict a failure envelope in close agreement with the known concrete behaviour. Under biaxial compression/compression loading, all the contact models predict a much higher failure envelope than that observed experimentally in concrete.

In both approaches (U&H), the BL contact model predicts the best agreement in compression/compression loading, and the CFM contact model is the contact model whose predictions are further away from the known concrete experimental behaviour.

4.3. Additional Parametric Studies

Additionally, several parametric studies were carried out in order to assess if the contact softening-based model agreement with the known concrete behaviour under biaxial compressive loading could be improved if the contact models under assessment had similar tendencies. The following results were found:

- In all contact models under assessment, an increase in the normal-to-stiffness ratio leads to a better agreement with the known concrete biaxial compressive loading failure envelope. It should be noted that this improvement in the predicted response is due to the worst prediction of the macroscopic Poisson's coefficient;
- With a reduction in the number of working contacts, by setting cohesionless contacts given a certain contact area threshold, a better response is obtained with all contact softening-based models. The better agreement is more noticeable with the BL contact model and with the LSSB contact model following a heterogeneous (H) approach. It should be stressed that with contact reduction, the proper macroscopic elastic behaviour is predicted with an increase in the normal-to-shear ratio.
- If a maximum contact compressive strength of 60.0 MP is adopted, both the BL and the LSSB contact models predict, under biaxial compressive loading, a failure envelope closer to the known concrete behaviour. A similar result is expected to occur with a CFM contact model if a compression cap is adopted. It should be mentioned that with the LSSB contact model under uniaxial compressive loading, the adoption of maximum compressive strength of the order of 60.0 MPa leads to an increase in the post-peak ductility that does not occur in concrete and is not predicted with a BL-Y contact model;
- If a PCM is adopted, the failure envelope predicted with a BL contact model under biaxial loading is of the same order as the failure envelope predicted when moment transmission is considered, whereas for the LSSB contact model and the CFM contact models, the failure envelope predicted with a PCM under biaxial compression loading is smaller than the failure envelope predicted when moment transmission is considered. Note that with all contact models, a maximum macroscopic compressive strength-to-tensile strength of 6 to 8 is predicted with a uniform approach (U) when a PCM is adopted;

- If a PCM and a normal-to-shear stiffness ratio of 0.50 are adopted, all contact-based models under assessment predict a biaxial failure envelope in close agreement with the known concrete behaviour, especially the BL and LSSB contact models. It can be highlighted that with a PCM, a 60% computational time reduction is obtained when compared with a 3D PM that considers moment transmission;
- For all softening-based contact models and for all modelling approaches, it is possible to carry out a two-step calibration procedure that greatly reduces the required computational times: an initial estimate of the best-fit parameters can be found using a coarser assembly, and then a localized search can be carried out with a refined PM.

4.4. Final Conclusions and Further Work

This paper highlights that the BL contact model can be used with confidence in PM fracture studies with the following advantages in detailed 3D PM DEM-based models:

- Reduced number of contact strength parameters requiring calibration. In addition, the relationship between the macroscopic properties and the contact properties is more straightforward than the one that occurs with the CFM contact model;
- Lower associated computational costs. Compared with the BL contact model, the LSSB contact model has an associated computational cost that is 50% higher and the CFM contact model has an associated computational cost that is 15% higher;
- It predicts, for the best-fit properties that are found using uniaxial tests, the best agreement with concrete observed biaxial behaviour.

To improve the agreement with known concrete behaviour under biaxial loading, a compression cap needs to be included in the BL contact model. The LSSB contact model is also shown to be a valid option for concrete fracture studies, with the advantage of including a stress–strain boundary for high compressive stresses, but the computational costs are much higher than with the BL contact model. The CFM contact model is the most complex model to be implemented within a DEM-based PM. The CFM also requires the consideration of a compression cap and needs a normal-to-shear stiffness ratio closer to 1.0 for the best agreement with concrete biaxial behaviour, which cannot be adopted in PM studies if Poisson's ratio is to be properly approximated.

Further work is underway to validate the adopted 3D PM model to larger structures pursuing hybrid FEM/DEM models, where a finite element discretization is used in the zones where elastic behaviour is expected to occur. In addition, an evolution algorithm is also being developed to automatically calibrate the strength properties in uniaxial and biaxial loading conditions. Given the computational costs, which are quite relevant in both approaches, the BL model is an efficient and accurate modelling option.

Author Contributions: Conceptualization, N.M.A.; methodology, N.M.A. and M.L.B.F.; software, N.M.A. and S.O.; validation, N.M.A., M.L.B.F. and S.O.; writing—original draft preparation, N.M.A.; writing—review and editing, N.M.A., M.L.B.F. and S.O.; supervision, N.M.A.; project administration, N.M.A. and M.L.B.F. All authors have read and agreed to the published version of the manuscript.

Funding: This research received no external funding.

Data Availability Statement: The original contributions presented in the study are included in the article, further inquiries can be directed to the corresponding authors.

Acknowledgments: This study presented here is part of the research project StepDam: A step forward for the ability to anticipate and prevent failures of concrete dam foundations, supported by LNEC.

Conflicts of Interest: The authors declare no conflicts of interest.

References

1. Potyondy, D.; Cundall, P. A bonded-particle model for rock. *Int. J. Rock Mech. Min.* **2004**, *41*, 1329–1364. [CrossRef]
2. Zhang, S.; Zhang, D.; Zhao, Q.; Chi, M.; Zhang, W.; Yu, W. DEM Investigation of the Influence of Minerals on Crack Patterns and Mechanical Properties of Red Mudstone. *Processes* **2019**, *7*, 162. [CrossRef]

3. Scholtès, L.; Donze, F. A DEM model for soft and hard rocks: Role of grain interlocking on strength. *J. Mech. Phys. Solids* **2013**, *61*, 352–369. [CrossRef]
4. Ye, Y.; Thoeni, K.; Zeng, Y.; Buzzi, O.; Giacomini, A. A novel 3D clumped particle method to simulate the complex behaviour of rock. *Int. J. Rock Mech. Min.* **2019**, *120*, 1–16. [CrossRef]
5. Sheikhpourkhani, A.; Bahaaddini, M.; Oh, J.; Masoumi, H. Numerical study of the mechanical behaviour of unwelded block in matrix rocks under direct shearing. *Bull. Eng. Geol. Environ.* **2023**, *83*, 22. [CrossRef]
6. Monteiro Azevedo, N. A Rigid Particle Discrete Element Model for the Fracture Analysis of Plane and Reinforced Concrete. Ph.D. Thesis, Heriot-Watt University, Edinburgh, UK, 2003.
7. Hentz, S.; Daudeville, L.; Donzé, V. Identification and validation of a discrete element model for concrete. *J. Eng. Mech.* **2004**, *130*, 709–719. [CrossRef]
8. Suchorzewski, J.; Tejchman, J.; Nitka, M. Discrete element method simulations of fracture in concrete under uniaxial compression based on its real internal structure. *Int. J. Damage Mech.* **2018**, *27*, 578–607. [CrossRef]
9. Sinaie, S.; Ngo, T.D.; Nguyen, V.P. A discrete element model of concrete for cyclic loading. *Comput. Struct.* **2018**, *196*, 173–185. [CrossRef]
10. Wang, P.; Gao, N.; Ji, K.; Stewart, L.; Arson, C. DEM analysis on the role of aggregates on concrete strength. *Comput. Geotech.* **2020**, *119*, 103290. [CrossRef]
11. Hentz, S.; Daudeville, L.; Donze, F. Discrete Element Modeling of a Reinforced Concrete Structure. *J. Mech. Behav. Mater.* **2009**, *19*, 249–258. [CrossRef]
12. Monteiro Azevedo, N.; Lemos, J.V.; Almeida, J. A discrete particle model for reinforced concrete fracture analysis. *Struct. Eng. Mech.* **2010**, *36*, 343–361. [CrossRef]
13. Thavalingam, A.; Bicanic, N.; Robinson, J.I.; Ponniah, D.A. Computational framework for discontinuous modelling of masonry arch bridges. *Comput. Struct.* **2001**, *79*, 1821–1830. [CrossRef]
14. Monteiro Azevedo, N.; Pinho, F.F.S.; Cismaşiu, I.; Souza, M. Prediction of Rubble-Stone Masonry Walls Response under Axial Compression Using 2D Particle Modelling. *Buildings* **2022**, *12*, 1283. [CrossRef]
15. Peng, Y.; Xu, Y.-R.; Zhang, X.-F.; Meng, H.-L.; Lu, X.-Y. Investigation on the effects of asphalt mixes and their combinations on asphalt mix shear strength by 3D discrete element method. *Int. J. Pavement Eng.* **2023**, *24*, 2251078. [CrossRef]
16. Liu, G.; Qian, Z.; Wu, X.; Chen, L.; Liu, Y. Investigation on the compaction process of steel bridge deck pavement based on DEM-FEM coupling model. *Int. J. Pavement Eng.* **2023**, *24*, 2169443. [CrossRef]
17. Wang, P.; Yin, Z.Y.; Wang, Z.Y. Micromechanical Investigation of Particle-Size Effect of Granular Materials in Biaxial Test with the Role of Particle Breakage. *J. Eng. Mech.* **2021**, *148*, 04021133. [CrossRef]
18. Wang, P.; Yin, Z.-Y.; Hicher, P.-Y.; Cui, Y.-J. Micro-mechanical analysis of one-dimensional compression of clay with DEM. *Int. J. Numer. Anal. Method. Geomech.* **2023**, *47*, 2706–2724. [CrossRef]
19. Mokhatar, S.N.; Sonoda, Y.; Kueh, A.B.H.; Jaini, Z.M. Quantitative impact response analysis of reinforced concrete beam using the Smoothed Particle Hydrodynamics (SPH) method. *Struct. Eng. Mech.* **2015**, *56*, 917–938. [CrossRef]
20. Liu, Z.; Liu, J.; Xie, X.; Zhen, M.; Wang, Y.; Ou, C.; Zheng, H. Material Point Simulation Method for Concrete Medium Fracture and Fragmentation under Blast Loading. *Appl. Sci.* **2023**, *13*, 8533. [CrossRef]
21. Schüler, T.; Jänicke, R.; Steeb, H. Nonlinear modeling and computational homogenization of asphalt concrete on the basis of XRCT scans. *Constr. Build. Mater.* **2016**, *109*, 96–108. [CrossRef]
22. Nitka, M.; Tejchman, J. A three-dimensional meso-scale approach to concrete fracture based on combined DEM with μCT images. *Cem. Concr. Res.* **2018**, *107*, 11–29. [CrossRef]
23. Yang, Z.J.; Li, B.B.; Wu, J.Y. X-ray computed tomography images based phase-field modeling of mesoscopic failure in concrete. *Eng. Fract. Mech.* **2019**, *208*, 151–170. [CrossRef]
24. Ghazvinian, E.; Diederichs, M.; Quey, R. 3D Random Voronoi grain-based models for simulation of brittle rock damage and fabric-guided micro-fracturing. *J. Rock Mech. Geotech. Eng.* **2014**, *6*, 506–521. [CrossRef]
25. Nikita, M.; Tejchman, J. Modelling of concrete behaviour in uniaxial compression and tension with DEM. *Gran. Matter.* **2015**, *17*, 145–164.
26. Lilliu, G.; Van Mier, M. 3D lattice type fracture model for concrete. *Eng. Fract. Mech.* **2003**, *70*, 927–941. [CrossRef]
27. D'Addetta, G.; Kun, F.; Ramm, E. On the application of a discrete model to the fracture process of cohesive granular materials. *Granul. Matter* **2002**, *4*, 77–90. [CrossRef]
28. Bazant, Z.; Tabbara, M.; Kazemi, M.; Cabot, G. Random particle model for fracture of aggregate or fiber composites. *J. Eng. Mech.* **1990**, *116*, 1686–1705.
29. Nagai, K.; Sato, Y.; Ueda, T. Mesoscopic simulation of failure of mortar and concrete by 3D RBSM. *J. Adv. Concr. Technol.* **2005**, *3*, 385–402. [CrossRef]
30. Hwang, Y.K.; Bolander, J.E.; Lim, Y.M. Evaluation of dynamic tensile strength of concrete using lattice-based simulations of spalling tests. *Int. J. Fract.* **2020**, *221*, 191–209. [CrossRef]
31. Candeias, M.; Monteiro Azevedo, N.; Farinha, L. VGCM3D—A 3D rigid particle model for rock fracture following the Voronoi tessellation of the grain structure: Formulation and Validation, In Proceedings of the V International Conference on Particle-Based Methods Fundamentals and Applications, Hannover, Germany, 26–28 September 2017.

32. Cusatis, G.; Bazant, Z.; Cedolin, L. Confinement-shear lattice model for concrete damage in tension and compression. *J. Eng. Mech.* **2003**, *129*, 1439–1448. [CrossRef]
33. Caballero, A.; William, K.J.; Carol, I. Consistent tangent formulation for 3D interface modelling of cracking/fracture in quasi-brittle materials. *Comput. Methods Appl. Mech. Eng.* **2008**, *197*, 2804–2822. [CrossRef]
34. Caballero, A.; Carol, C.; López, Z. A meso-level approach to the 3D numerical analysis of cracking and fracture of concrete materials. *Fatigue Fract. Eng. Mater. Struct.* **2006**, *29*, 979–991. [CrossRef]
35. Cundall, P. Distinct element models for rock and soil structure. In *Analytical and Computational Methods in Engineering Rock Mechanics*; Brown, E.T., Ed.; Chapter 4; Allen & Unwin: London, UK, 1987; pp. 129–163.
36. Vonk, R. *A micromechanical Investigation of Softening of Concrete Loaded in Compression*; Heron; Delft University of Technology: Delft, The Netherlands, 1993; Volume 38, pp. 1–94.
37. Zhang, J.; Ma, R.; Pan, Z.; Zhou, H. Review of Mesoscale Geometric Models of Concrete Materials. *Buildings* **2023**, *13*, 2428. [CrossRef]
38. Bazant, Z.P.; Xiang, Y.; Prat, P.C. Microplane model for concrete. I: Stress-strain boundaries and finite strain. *J. Eng. Mech.* **1996**, *122*, 245–254.
39. Cusatis, G.; Pelessone, D.; Mencarelli, A. Lattice discrete particle model (LDPM) for failure behavior of concrete. I: Theory. *Cem. Concr. Compos.* **2011**, *33*, 881–890. [CrossRef]
40. Hassanzadeh, M. Determination of fracture zone properties in mixed mode I and II. *Eng. Fract. Mech.* **1990**, *35*, 845–853. [CrossRef]
41. Kupfer, H.; Hilsdorf, H.K.; Rusch, H. Behavior of concrete under biaxial stresses. *ACI J.* **1969**, *66*, 656–666. [CrossRef]
42. Kazerani, T.; Yang, Z.Y.; Zhao, J. A discrete element model for predicting shear strength and degradation of rock joint by using compressive and tensile test data. *Rock Mech. Rock. Eng.* **2012**, *45*, 695–709. [CrossRef]
43. Liu, X.; Wang, Q.; Wang, Y.; Dong, Q. Review of calibration strategies for discrete element model in quasi-static elastic deformation. *Sci. Rep.* **2023**, *13*, 13264. [CrossRef] [PubMed]
44. Kibriya, G.; Orosz, Á.; Botzheim, J.; Bagi, K. Calibration of Micromechanical Parameters for the Discrete Element Simulation of a Masonry Arch using Artificial Intelligence. *Infrastructures* **2023**, *8*, 64. [CrossRef]
45. Monteiro Azevedo, N.; Lemos, J. A 3D generalized rigid particle contact model for rock fracture. *Eng. Comput.* **2013**, *30*, 277–300. [CrossRef]
46. Macorini, L.; Izzuddin, B.A. A non-linear interface element for 3D mesoscale analysis of brick-masonry structures. *Int. J. Numer. Meth. Eng.* **2011**, *85*, 1584–1608. [CrossRef]
47. Pulatsu, B. Coupled elasto-softening contact models in DEM to predict the in-plane response of masonry walls. *Comput. Part. Mech.* **2023**, *10*, 1759–1770. [CrossRef]